Modeling Study of Synergistic Effects Between Lower Hybrid and Electron Cyclotron Current Drive on EAST

S. G. Baek[1*], M. H. Li[2], W. Choi[3], P. T. Bonoli[1], B. J. Ding[2*], A. Garofalo[3], G. M. Wallace[1], M. Wang[2], H. Xu[2], Q. Zang[2], and H. Zhao[2]

[1]MIT Plasma Science and Fusion Center, Cambridge, USA
[2] Institute of Plasma Physics, Chinese Academy of Sciences, Hefei, China
[3] General Atomics, San Diego, USA

*Corresponding authors: sgbaek@psfc.mit.edu, bjding@ipp.ac.cn

Abstract

Recent radio frequency (RF) current drive experiments in EAST provide an opportunity to investigate RF synergy effects between Electron Cyclotron (EC) and Lower Hybrid (LH) current drive. Synergy current is the excess current that can arise from overlapping two wave-particle resonance bands in the velocity phase space. In this work, a ray-tracing and Fokker-Planck code package, GENRAY/CQL3D, is used to model and investigate the phase space interaction of two waves for EAST. The target plasma features a high central electron temperature of 6.5 keV, promoting Landau damping of the LH power on-axis that overlaps with the EC power resonance region. The GENRAY/CQL3D code evaluates a self-consistent electron distribution function in the presence of two RF quasilinear diffusion coefficients. A systematic scan in collisional dissipative LH power loss and fast-electron radial transport is performed. Including the divertor SOL in GENRAY and fast-electron radial diffusion in CQL3D can quantitatively provide model total RF currents in line with the experimental range. Radial transport operator broadens and smooths the radial region of synergistic current generation. The impact of LH wave scattering on the synergistic interaction is examined by introducing the LH wave scattering angle in a heuristic manner. The sensitivity analysis is presented. Furthermore, a numerical scan of the ECCD injection angles is conducted to evaluate the synergistic interactions. The roles of LHCD and ECCD in synergistic current generation are further examined through a power scan of both power sources.

1. Introduction

External heating and current drive are critical on tokamaks for developing non-inductive scenarios and for profile control to access advanced regimes toward high-performance operation. In addition to neutral beam power, microwave radio frequency (RF) powers are an attractive current drive source on tokamaks for their technology maturity and physics advantages. Lower hybrid current drive (LHCD) [1,2], for example, is known to exhibit the highest current drive efficiency and has been demonstrated in a number of tokamak experiments [3]. The highest efficiency demonstrated is due to its wave-particle interactions occurring along the parallel direction to the background magnetic field via Landau damping of LH waves with the resonant electrons at a relatively high phase velocity ($v_{\parallel} \approx 3v_{te}$ where v_{te} = $(2T_e / m_e)^{1/2}$ is the thermal velocity). LHCD has been proposed as an off-axis current drive actuator in several reactor studies [4,5], which is compatible with a reactor scenario that requires a large-radius internal transport barrier (ITB). In present-day experiments, control of the LHCD profile can be challenging due to low temperature, resulting in a centrally peaked broad profile [6,7]. Meanwhile, electron cyclotron current drive [2] is another well-established application for current drive and stability control. Its cyclotron resonance mechanism makes precise control in power deposition location easily

achievable, and ECCD is widely utilized in the present experiments and proposed as a key RF actuator in future reactors. However, its theoretical current drive efficiency is 75% of the LHCD efficiency due to a wave-particle interaction occurring along the perpendicular direction. Moreover, its efficiency further deteriorates quickly off-axis due to the trapping effect [8].

An investigation has been sought in the past to optimize the interaction between ECCD and LHCD. In particular, the theoretical study of the interaction of the two waves in the velocity phase space led to the identification of the synergistic current [9], an additional current that can arise due to the overlapping of two wave-resonance regions in the phase space. In the early 2000s, a synergistic interaction was used in FTU experiments [10,11] to access the internal-transport-barrier advanced scenario regime. It is reported that the EC efficiency in the presence of LHCD can approach that of LHCD and good agreement with kinetic modeling was demonstrated. It was also experimentally demonstrated on Tore Supra [12] that the synergy factor, defined as $F_{syn} = \Delta I/I_{EC}$ where $\Delta I = I_{LH+EC} - I_{LH}$, was found to approach 4 with the extra synergy current up to 120 kA. Here, I_{LH} and I_{EC} are individual LH and EC currents, I_{LH+EC} is the total current that includes the synergistic current (I_{syn}), and F_{syn} is the ratio of the sum of the EC and synergy currents ($I_{EC}+I_{syn}$) to the EC current only (I_{EC}), with a view that the synergistic interaction contributes to an increase in the ECCD efficiency.

This paper presents a modeling analysis of the interaction between ECCD and LHCD using the EAST parameters. EAST is a superconducting tokamak in China with its mission to establish a physics and engineering basis for a tokamak reactor. As the RF heating and current drive actuators are maturing in terms of power and types at EAST, there is a growing interest in optimizing the combination of these RF actuators to access the advanced tokamak regime. Experimentally, the heating effects of the EC power on the LHCD profile have recently been characterized [13]. A synergistic interaction between the lower hybrid waves at two different frequencies is investigated extensively in both experiments and theory and modeling [14,15]. Also, integrated modeling now includes various RF actuators for experimental interpretation and for scenario prediction [16]. So far, a synergistic interaction between LHCD and ECCD in the kinetic space has not yet been routinely integrated into predictive modeling. It is, therefore, important to study EAST plasmas to quantify such an interaction and identify a scenario in which such an interaction becomes significant. It is also important to explore scenarios that can benefit from the optimal utilization of RF actuators for achieving advanced tokamak operation.

For this purpose, this paper conducts a time-slice kinetic modeling analysis of the synergistic interaction using the wave and plasma parameters of the EAST discharge, #106904, and examines synergy current generation under various conditions. In this plasma, both LHCD and ECCD were available at a moderate power level, and the LH deposition location is expected to overlap with the EC resonance layer in the on-axis region due to a high central temperature (~6.5 keV). This experimental condition is unique because a high central temperature is expected to facilitate single-pass damping of the injected LH wave power. Its interaction with ECCD is expected to be optimal as well. In the analysis, collisional dissipation of the LH wave power and fast electron spatial diffusion of both the LH- and EC-driven fast electrons are incorporated into the ray-tracing and Fokker-Planck analysis to estimate the synergistic current from the model under various conditions. CQL3D allows the construction of a self-consistent RF quasi-linear diffusion operator, along with a model spatial diffusion operator. Additionally, the impact of LH wave scattering on synergistic current generation is examined by introducing the scattering effect in an ad-hoc manner. LH wave scattering by edge/SOL turbulence was found to have a profound effect on the up-shift mechanism of the LH parallel refractive index ($n_{||}$), better reproducing the experimental LHCD

profile in low- to moderate-temperature plasmas by promoting on-axis power damping. While several models exist to capture this effect, this paper conducts an angular scan of the perpendicular LH wavevector with respect to the flux-surface normal vector at the initial launch point. The level of synergistic current generation and its spatial profile are examined. Furthermore, two ECCD injection angles, toroidal and poloidal injection angles, are also systemically scanned in the ray-tracing analysis to estimate the range of synergistic current generation expected in the EAST parameter space. The dependence of synergy current on the ECCD and LHCD powers is also analyzed.

The organization of the paper is as follows: Section 2 presents the experimental condition of the EAST plasma #106904. Section 3 performs kinetic modeling of the LHCD-only case and then of the combined LHCD and ECCD scenario, including the effects of collisional absorption and fast electron diffusion. Section 4 performs a sensitivity study of the synergistic interaction in the presence of the LH wave scattering effect. Section 5 examines the variation of synergistic current generation through parametric scans of the ECCD injection angles, along with a discussion on the impact of varying EC and LH power levels. Finally, Section 6 provides a summary and conclusion.

2. Experimental Condition

EAST is one of the few operating tokamaks that can experiment and demonstrate a long pulse operation in a high-performance advanced operation scenario, characterized by a high level of bootstrap current with profile tailoring. The major radius is R_0 = 1.85 m, and the minor radius is a = 0.45 m. The main heating and current drive actuators on EAST are two LHCD systems at 2.45 GHz and 4.6 GHz [17]. In Discharge #106904, only the 4.6 GHz LHCD system is utilized due to its higher observed efficiency. The 4.6 GHz source power is up to 6 MW with 24 klystrons rated at 250 kW each. The power is coupled to the plasma with a fully-active-multijunction antenna, which allows precise control of antenna phasing. Frequency-dependent parasitic losses attributed to parametric decay instabilities have been observed at 2.45 GHz [18,19].

The EC system at 140 GHz is another major RF actuator on EAST [20]. The frequency corresponds to the 2nd harmonic resonance at the magnetic axis. Four gyrotrons have a total source power of up to 4 MW. Two horn antennas are used to couple this power to the plasma, with one of them being equipped with a steerable mirror. This mirror allows control of the EC power deposition location by adjusting the poloidal and toroidal injection angles. The RF actuators are equipped with water cooling, and their operation has been demonstrated in a continuous plasma operation for up to 1000 seconds [21,22].

Figure 1 illustrates the time history of the plasma discharge of interest, #106904. The magnetic field is B_{t0} = 2.44 T, and the total plasma current is 320 kA. The line averaged density is $\bar{n}_e \approx 1.8\text{x}10^{19}$ m^{-3}, and the effective ion charge is Z_{eff} = 3.5 from the visible Bremsstrahlung emission measurement, assuming a flat Z_{eff} profile. In the first part of the discharge (t < 60 sec.), the plasma current is sustained solely by LHCD, except for the bootstrap current of 76 kA evaluated from Sauter's model in the GENRAY/CQL3D code package [23,24]. The peak parallel refractive index of the LH spectrum is $n_{\parallel}$ = 2.04, corresponding to a 90-degree phasing angle difference between adjacent waveguides in the LH antenna.

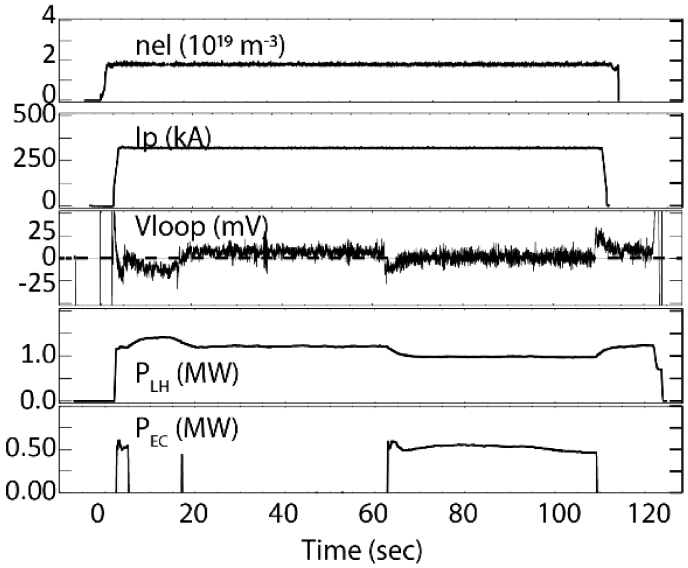

Figure 1: Time histories of the plasma parameters of the EAST discharge #106904: line-averaged density, plasma current, loop voltage, LH power, and EC power.

The LH power was feedback-controlled to sustain a non-inductive plasma operation, while an error in the controller led to over current drive at the beginning of the discharge. As shown in the loop voltage trace in Figure 1, in the first 20 seconds, the applied LH power at P_{LH} = 1.42 MW results in a current overdrive, as indicated by the negative loop voltage of V_{loop} ≈ -0.13 mV. Then, a reduction in LH power to P_{LH} = 1.21 MW for the time range from t = 20 seconds to t = 60 seconds resulted in the residual loop voltage increasing to V_{loop} ≈ 6 mV. For the purpose of analysis in this paper, a linear interpolation of the two powers is used to estimate the LH power needed for the non-inductive operation (P_{LH} = 1.28 MW).

In the latter period of the discharge, after t > 60 seconds, the addition of ECCD power, P_{EC} = 0.55 MW, lowers the LH power requirement to P_{LH} = 0.98 MW to maintain the zero-loop voltage. The toroidal and poloidal injection angles in the EC system are α = 200° and β = 77°, respectively. This angle pair corresponds to the on-axis current drive with the parallel refractive index of $n_{\parallel,EC}$ ≈ 0.4. Figure 2 shows the orientation of the two injection angles. The toroidal injection angle, α, is the ECCD orientation with respect to the toroidal plane. Similarly, the poloidal injection angle, β, is the ECCD orientation defined in the poloidal plane. The toroidal injection angle can be varied from 155° to 205°, while the poloidal injection angle can be varied from 65° to 95°. Because the ECCD efficiency is lower than the LHCD efficiency, the total power requirement to sustain the same non-inductive plasma in #106904 is increased from P_{tot} = 1.28 MW to P_{tot} = 1.43 MW. The aim of the analysis here is to evaluate the synergistic interaction between the two waves. The current profile is expected to be fully relaxed in each phase. The current relaxation time scale [25] is $\tau_{CR} \approx \frac{1.4a^2T_e^{1.5}}{Z_{eff}}$ ≈ 1.2 seconds for a = 0.45 m, T_e = 6 keV, and Z_{eff} = 3.5, where a is the minor radius.

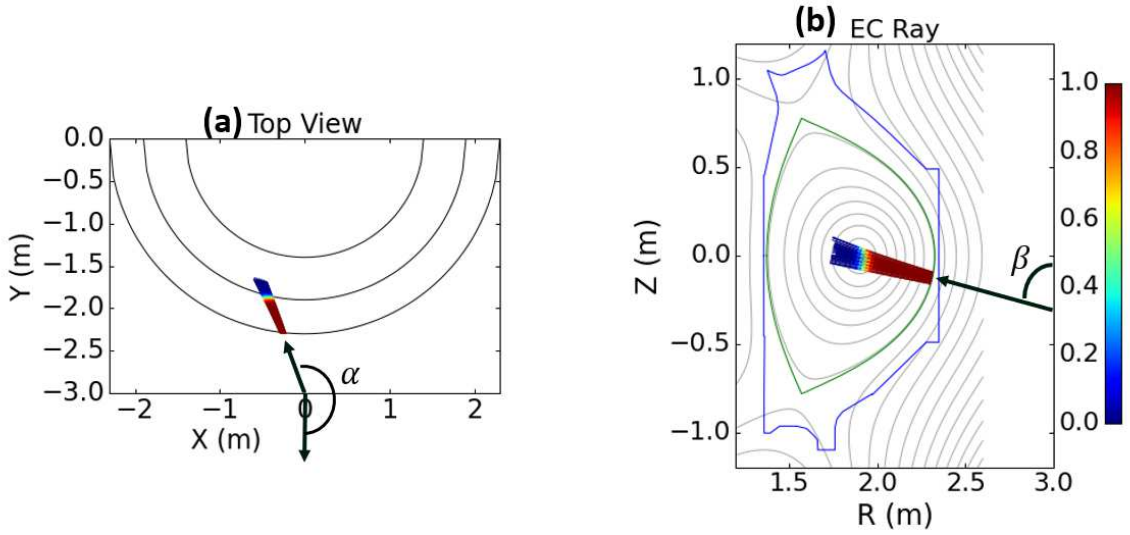

Figure 2. An example of the (a) top view and (b) poloidal view of the EC ray trajectories. The toroidal injection angle (α) and the poloidal injection angle (β) are also shown. For Discharge #106904, α = 200° and β = 77°. The last optic element, the steerable plane mirror, is located at (R, Z) = (3.0 m, −0.3 m).

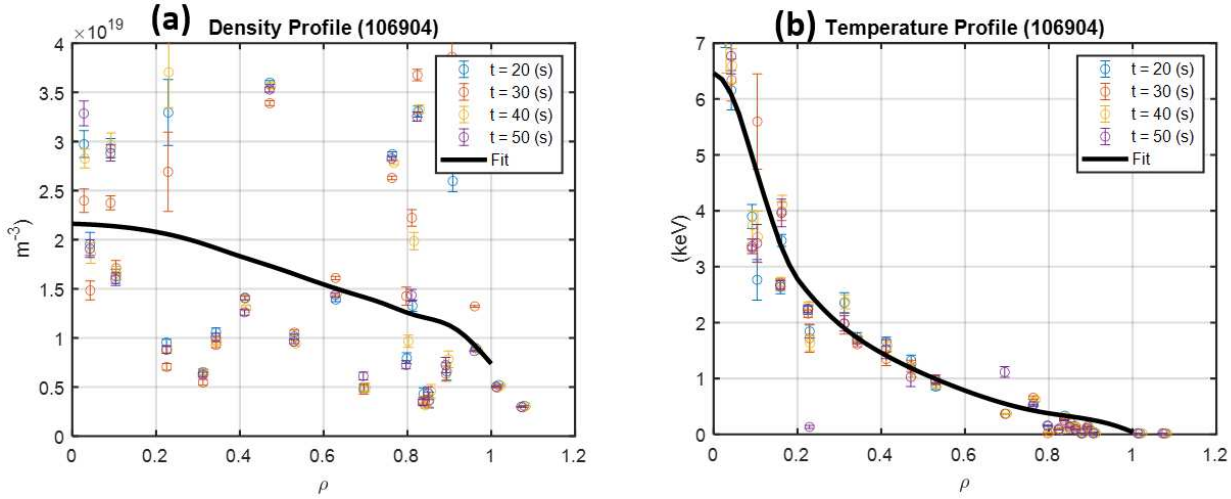

Figure 3: Thomson measurements of (a) electron density profile and (b) electron temperature profile for LH-only phase in Discharge, #106904 (t < 60 sec). The best-fit curves, based on the measurements at t = 20, 30, 40, and 50 seconds, are shown in black in both profiles.

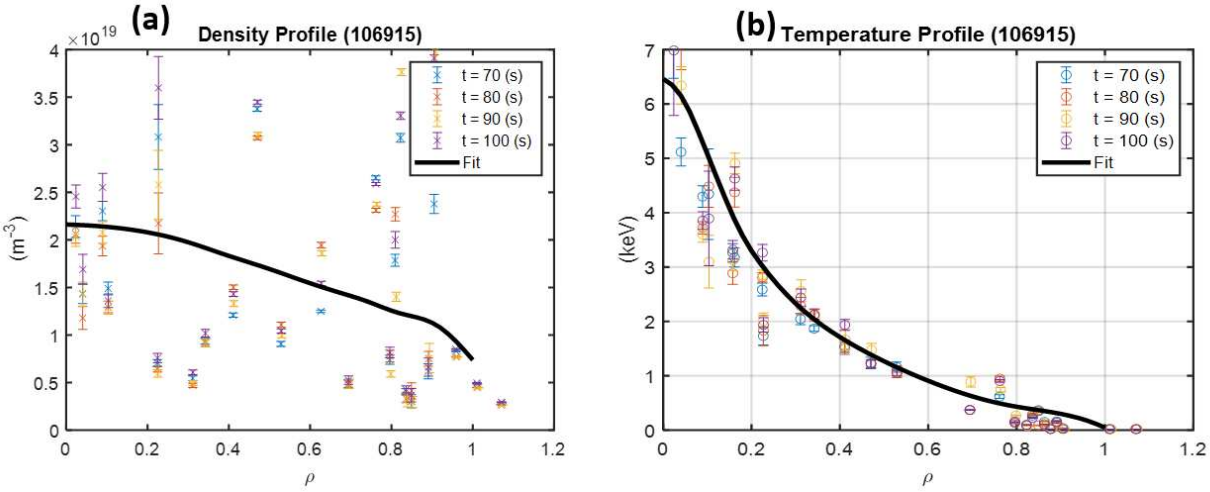

Figure 4. Thomson measurements of (a) electron density profile and (b) temperature profile adopted from #106915 for input to model the LH-EC phase in Discharge, #106904. The best-fit curves, based on the measurements at t = 70, 80, 90, and 100 seconds, are shown in black in both profiles. Discharge #106915 is a similar discharge to Discharge #106914.

Figure 3 and Figure 4 display the electron density and temperature profiles used in the analysis, as measured with the Thomson scattering diagnostic, for the LH-only and LH-EC phases, respectively. For the Thomson profile for the LH-EC phase, the measurements are taken from another discharge, #106915, which closely matches #106914 in terms of plasma parameters and input powers. Thomson data were not available during the LH-EC phase in #106914, while #106915 has the combined LH and EC powers only. In both cases, there is a large scatter in the density measurements, and the same best fit is applied, which is a limitation of the analysis. Note that this run day was devoted to demonstrating a long-pulse steady-state plasma [22]. The density is kept relatively low to enable RF operation at a low level while ensuring the characterization of the effects of the external current drive. For the temperature profiles, the scatter in the error bar is significantly reduced. The central electron temperature is centrally peaked at $T_{e0} \approx 6.5$ keV. A linear dependence of LHCD efficiency on temperature has previously been documented [26]. During the LH-EC phase, a slightly higher level of temperatures is measured in the inner half of the plasma inside $\rho \approx 0.2$, compared to the LH-only phase. Meanwhile, the on-axis temperature remains nearly the same within the error bars. This high central temperature ensures that the Landau damping condition is satisfied with modest up-shifts of the wave $n_{\parallel}$ for the given LHCD input spectrum ($n_{\parallel} > 5 - 7/\sqrt{T_e}$), thereby enhancing power damping on the first pass. It helps minimize parasitic edge interactions as well.

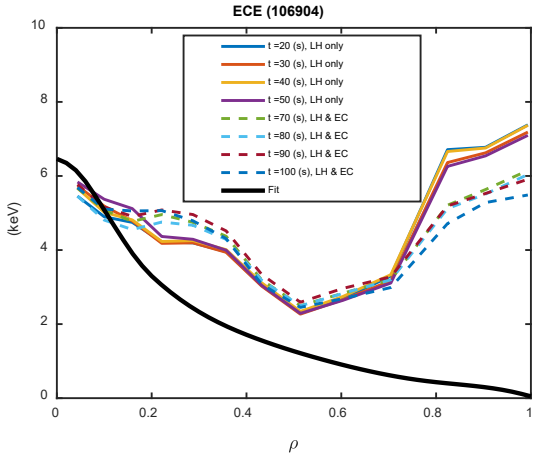

Figure 5: Radial profiles of the electron cyclotron emission of the EAST discharge #106904 at different time slices, covering both the LHCD-only (t < 60 sec) and the combined LHCD/ECCD phase (t > 60 sec). The fit of the Thomson temperature profile is also shown in black.

Figure 5 shows the corresponding radial profile of the electron temperature measured using the electron cyclotron emission (ECE) diagnostic in #106904 at eight different time points, including the LHCD-only (t < 60 seconds) and the combined LHCD/ECCD phases (t > 60 seconds). A fitted Thomson temperature profile is shown as a reference profile. The ECE measurement is heavily polluted by the LH-driven non-thermal ECE across the plasma. Only a limited number of core channels inside ρ < 0.1 measures a temperature comparable to the Thomson measurement. When ECCD power replaces a portion of the LHCD power (after t = 60 seconds), the ECE profile exhibits a decreased level of non-thermal emission at the edge and an increased level of non-thermal ECE near ρ ≈ 0.3, which could indicate a higher level of fast electron populations in the internal region. Nevertheless, Figure 3 and Figure 4 suggest that the ECCD power drives non-inductive currents with a minimal heating effect, thereby facilitating LHCD analysis. The next section analyzes the contributions from LH, EC, and synergy currents using kinetic modeling.

3. Kinetic modeling

In this study, a ray-tracing/Fokker-Planck code package, GENRAY/CQL3D [23,24], is used for current drive modeling. The magnetic equilibrium is from the EFIT magnetic reconstruction code [27]. The π-Scope, a Python-based workbench, is used to facilitate code input preparation, code execution, and output data process and visualization [28]. GENRAY is a 3D ray tracing code that solves wave propagation and absorption in a geometrical limit. The RF wave data evaluated in GENRAY, including ray trajectory, parallel and perpendicular refractive indices, and wave polarization, are crucial for defining the location and magnitude of wave-particle interaction in the velocity phase space. CQL3D is a bounce-averaged Fokker-Planck solver that evaluates an electron distribution function by balancing RF diffusion against the background Coulomb collisional diffusion. In a simple form, the Fokker-Planck equation can be written [24,29]:

$$\frac{\partial f_e}{\partial t} + \nabla \cdot \vec{S}_w - \sum_s C(f_e, f_s) = 0 \quad (1)$$

where f_e is the electron distribution function, $\vec{S}_w$ is the wave-induced flux, and $C(f_e, f_s)$ is the collision term depicting a collisional process between species, here evaluated over the electrons and ions. The collision operator relaxes the distribution function to Maxwellian in the absence of the RF source. From the quasi-linear theory [1,30], the RF-induced electron flux S_w is described as a diffusion process in the phase space:

$$\vec{S}_w = -\vec{\vec{D}}_w \cdot \nabla f_e$$

where $\vec{\vec{D}}_w$ is the quasilinear diffusion coefficient tensor. For LHCD, the diffusion occurs in the parallel direction: $\vec{\vec{D}}_{LH} = D_{\parallel\parallel}\hat{v}_\parallel\hat{v}_\parallel$. For ECCD, it is in the perpendicular direction: $\vec{\vec{D}}_{EC} = D_{\perp\perp}\hat{v}_\perp\hat{v}_\perp$. As a key point of the analysis in this paper, both quasi-linear diffusion coefficients are simultaneously considered in CQL3D to model the self-consistent evolution of the electron distribution function and, therefore, the synergy current generation. Using the GENRAY data, CQL3D constructs the quasilinear diffusion coefficient in a finite region of the phase space where the wave-particle resonance condition is satisfied:

$$\omega - k_\parallel v_\parallel - n\omega_c/\gamma = 0$$

Here, ω is the wave frequency in radians, $k_\parallel$ is the parallel wavenumber, $v_\parallel$ is the parallel particle velocity, n is the order of the cyclotron harmonic interaction, ω_c is the cyclotron frequency in radians, and γ is the relativistic factor. CQL3D also allows including a model radial diffusion operator, which will be discussed below. CQL3D iteratively solves the Fokker-Planck equation to find a self-consistent electron distribution function.

3.1. LHCD modeling

In this subsection, wave modeling during the LHCD-only phase (t < 60 sec. in Figure 1) is considered. During the LHCD-only phase, the experimental power launched is 1.28 MW. Figure 6 shows the LH power spectrum from the ALOHA antenna coupling code [31,32] using the 90 degree phasing difference between the adjacent grill waveguides. A typical antenna density of $7\text{x}10^{17}$ m^{-3} is assumed. The experimental reflection coefficient at ~ 2% agrees with the model value of ~ 1%. The primary lobe at a peak phasing of the parallel refractive index, $n_\parallel$ = -2.04, contains 62% of the total power. The 12 dominant lobes in the $n_\parallel$ range of -4 < $n_\parallel$ < -1, are included in the analysis, which accounts for 72% of the total power. Here, the negative sign indicates the current drive direction, which is opposite to the plasma current direction.

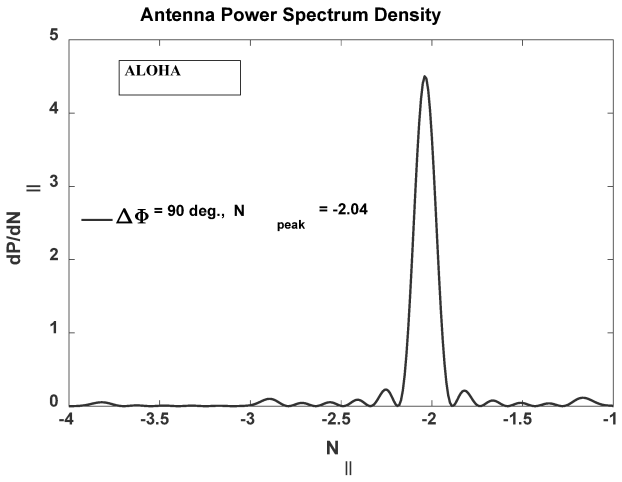

Figure 6. LHCD antenna spectrum for the 90° Phasing case on EAST for the range of -4 ≤ $n_{||}$ ≤ -1. The negative sign indicates the current drive direction, which is opposite to the plasma current direction.

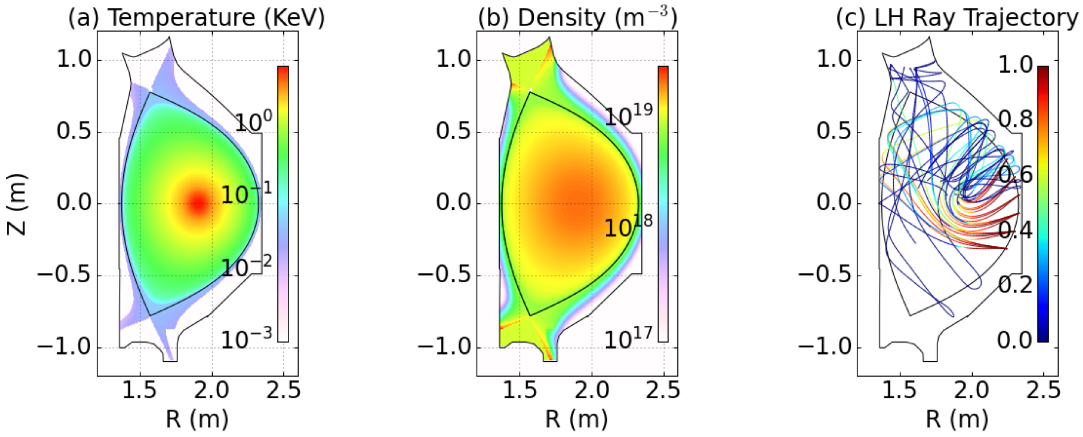

Figure 7. (a) 2D temperature and (b) density profiles as an input to GENRAY. Outside the LCFS (green curve), temperature and density distributions along each field line are computed from the two-point model. See the text for a description. With a rapid drop in the temperature near the divertor-end side, a rise in density is seen at that region due to pressure conservation on each flux tube. (c) Poloidal projection of the LH ray trajectories. The color bar denotes the normalized ray power. Because of the high density (10^{19} m^{-3}) and low temperature (1 eV) assigned to the private flux regions, the ray power is strongly attenuated and often terminated due to collisional dissipation in those regions.

To account for the EAST magnetic equilibrium and collisional losses, the two-point model for prescribing the density and temperature profiles in the SOL is adopted [33], as shown in Figure 7. The model uses the upstream (midplane side) and downstream (divertor side) density and temperature information to reconstruct the profiles on each flux tube, resulting in a realistic divertor SOL profile in the ray-tracing

analysis. At the outer midplane, exponentially decaying functions for density and temperatures are assumed with the following form:

$n_{e,\mathrm{mid}} = n_{e,\mathrm{LCFS}}\, e^{(\rho-1)/\sigma_n}$ and

$T_{e,\mathrm{mid}} = T_{e,\mathrm{LCFS}}\, e^{(\rho-1)/\sigma_t}$,

where ρ is the normalized radius, and σ_n and σ_t are the scaling lengths for density and temperature, respectively, normalized to the minor radius. The heat diffusion equation on each flux tube is solved with the Spitzer conductivity. Then, the density field is reconstructed by applying the constant pressure assumption, as determined by the midplane profile. In the private flux region, the constant high-density of 10^{19} m^{-3} and the low temperature of 1 eV are assigned. Figure 7 (c) shows that ray trajectories are terminated upon entering the private flux region due to strong collisional power attenuation. In GENRAY, the collisional power dissipation is evaluated by introducing the dissipation term in the electron mass: $m_e \rightarrow m_e (1+i\nu_{ei}/\omega)$, where ν_{ei} is the electron-ion collision frequency, which is proportional to $n_e/T_e^{1.5}$. Note that, in the CQL3D Fokker-Planck analysis, only the closed flux surfaces are considered, while the collisional dissipative power registered in GENRAY is still tallied.

$T_{e,min}$ (eV)	σ_t	$n_{e,min}$ (m^{-3})	σ_n	Landau Absorption (kW)	Collisional Absorption (kW)	I_{LH} (kA)
10	0.05	10^{17}	0.05	800 (95%)	45	361
5				792 (94%)	52	358
3				780 (92%)	65	353
1				690 (82%)	155	313

Table 1. Power partition between Landau and collisional absorptions and the driven LH current (I_{LH}) at four different minimum temperatures in the SOL outside the LCFS assumed in GENRAY. The LH current is evaluated without including the radial transport effect of fast electrons.

In the present analysis, most of the wave power is absorbed in the plasma core via Landau damping within a few passes due to a high center temperature. Table 1 shows the power partition between core Landau absorption and edge/SOL collisional absorption of the injected LH power for a given set of minimum temperatures at the SOL. The minimum SOL temperature is varied from 1 to 10 eV for the fixed e-folding length at the outer midplane σ_t = 0.05, corresponding to a typical e-folding length of ~2.5 cm on EAST as measured using a reciprocating probe. In our case, the impact of collisions becomes appreciable only at the low minimum SOL temperature of 1 eV because of strong single-pass damping and low density. Such a weak effect of collisional dissipation is compared to the high-density Alcator C-Mod plasmas (>10^{20} m^{-3}), in which a majority of the input LH power can be dissipated by edge/SOL collisions [34]. The predicted LH current is 313 kA with $T_{e,min}$ = 1 eV, while the experimental LHCD current after subtracting the bootstrap current is 257 kA. The scan in the minimum temperature shows that collisional power absorption alone over-predicts the experimental current and suggests that additional mechanisms may play a role.

In our analysis, anomalous radial transport of fast electrons is investigated. Previous studies on EAST indicate that including radial diffusion was critical for matching the magnitude and profile of the LHCD current [7]. An iterative solver in CQL3D solves the 3D-implicit (2D in momentum space and 1D in radial

space) Fokker-Planck equation. This implicit time advance allows a larger time step up to 0.1 msec, which was used while ensuring convergence between the powers in ray-tracing and Fokker Planck evaluations. The simulation was run for a total of 500 steps (50 msec), corresponding to approximately two to three slowing down times, thus allowing the current density profile to evolve to a steady state.

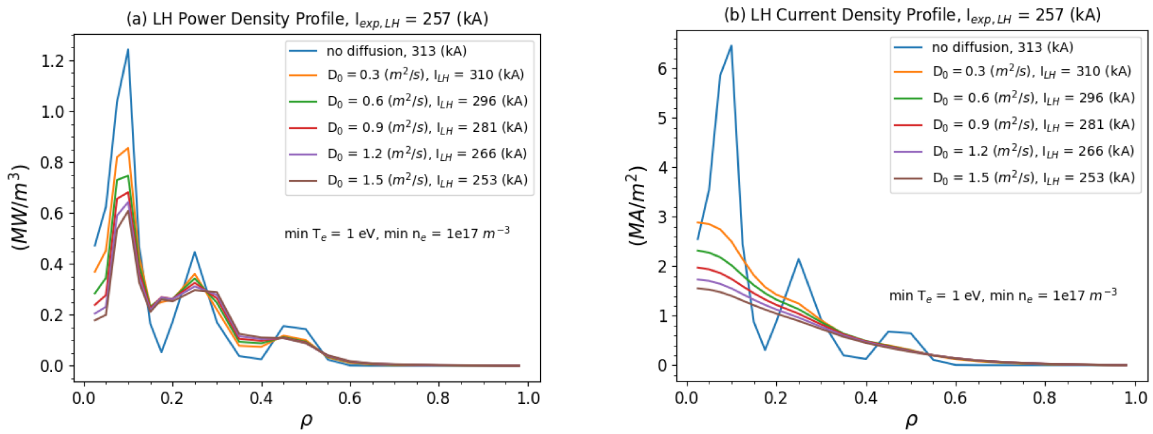

Figure 8. (a) LH power deposition and (b) current density profiles as a function of the central radial diffusion coefficient. The profiles are for the LHCD-only case. The experimental current is 257 kA after subtracting the bootstrap current contribution.

Figure 8 shows the LHCD power density and current profiles at various levels of the central radial diffusion coefficient, D_0. While the velocity- and radial- dependence of radial diffusion is unknown apriori, they are chosen to be dependent on electron parallel velocity and on the normalized radius, as adopted in the previous study [35]:

$$D_{rr} = D_0 \frac{v_\parallel / v_{te}}{\gamma^3} (1 + 3\rho^3) \frac{n_{e0}}{n_e(\rho)}$$

The velocity dependence accounts for the fast electron response to electromagnetic turbulence, and the inverse proportionality to the relativistic factor provides a cutoff mechanism to fast electron transport at high energy due to drift orbit effects [24]. Here, the radial- and density-dependences model an increased radial transport toward the plasma periphery. CQL3D internally adjusts an inward pinch velocity to conserve the density on each flux surface to the prescribed level. Figure 8 shows that the impact of radial transport broadens both the power and, more clearly, current density profiles and can lower the total driven LHCD current. As compared to the LH current of I_{LH} = 313 kA in the absence of the radial transport effect, the LHCD current is reduced to 253 kA, which is the level comparable to the experimental current, with a central diffusion coefficient of D_0 = 1.5 m^2/s. The resulting current density profile also peaked centrally and smoothly decreased toward the edge. Notably, even a small level of spatial diffusion at D_0 = 0.3 m^2/s is found to spread the current density profiles that are highly localized in space without radial transport.

Another interesting observation is that this diffusivity level at D_0 = 1.5 m^2/s lies in between the diffusivity estimated from EAST's low (L-mode) and high (H-mode) confinement times: $\tau_L \approx$ 16 msec and $\tau_H \approx$ 52 msec, respectively. These timescales yield a diffusion coefficient range from 0.67 m^2/s to 2.2 m^2/s, as

evaluated from the cylindrical limit: $D = a^2/5.78/\tau$, where a is the minor radius. In this section, the kinetic modeling analysis with a sensitivity scan in the edge SOL temperature and fast electron diffusivity finds that collisional dissipative loss is relatively weak in a high-temperature, low-density plasma due to a stronger core absorption compared to a multi-pass damping regime. Additionally, a finite diffusivity level of $D_0 \approx 1.5$ m^2/s, in line with the EAST parameter range, quantitatively reproduces the experimental LHCD current. The following section will examine the phase space interaction between LHCD and ECCD.

3.2. Modeling of phase space synergy between LHCD and ECCD

To model the synergy interaction, ray-tracing information from both LH and EC waves is transferred to CQL3D to construct a self-consistent RF quasi-linear diffusion coefficient. The EC ray information is evaluated in GENRAY in a manner similar to the LH case. The ECCD system used in Discharge #106904 is powered by two 140 GHz gyrotrons #1 and #2 on EAST. The X-mode EC waves are launched to the plasma from the low-field-side of the EAST tokamak, guided by the steerable mirror at (R, Z) = (3.0 m, −0.3 m), as shown in Figure 2 above.

Table 2 outlines a detailed breakdown of the RF current contributions for the combined injection of LH and EC powers as a function of the central radial diffusion coefficient. The same functional form is used for radial diffusion, and the central radial diffusion coefficient is varied from 0 to 2.1 m^2/s in steps of 0.3 m^2/s. Regarding the ECCD power, the transmission loss estimate of 10% is considered [36]. For this simultaneous injection case, the expected experimental total RF current is 244 kA after subtracting the bootstrap current contribution evaluated from the density and temperature profiles shown in Figure 4 above. To evaluate the synergistic current (I_{syn}) in each case, the simple sum of the two RF currents (I_{LH}+ I_{EC}) is subtracted from the total current (I_{LH+EC}) that is evaluated from the combined RF quasilinear diffusion coefficient. Two independent GENRAY/CQL3D simulations are run for LH-only and EC-only cases to separately calculate I_{LH} and I_{EC}. The table shows that the total RF current, I_{LH+EC}, is larger than the sum of the individual currents, $I_{LH} + I_{EC}$, by 20 ~ 30 kA, which is about 6 – 10 % of the total current. This difference is attributed to the synergy current, I_{syn}. With $D_0 = 2.1$ m^2/s, the modeled total RF current (I_{LH+EC}) can quantitatively match the experimental current expected (244 kA). Adopting Fidone's definition [9], the synergy factor is calculated as $F_{syn} = (I_{LH+EC} - I_{LH}) / I_{EC} = 1.8$ in this case.

D_0 (m^2/s)	I_{LH+EC} (kA)	I_{LH} (kA)	I_{EC} (kA)	I_{LH}+I_{EC} (kA)	I_{syn} (kA)	I_{syn} / I_{LH+EC} (%)
0	298	232	47	279	19	6
0.3	316	240	43	283	33	10
0.6	310	233	41	274	36	12
0.9	297	222	39	261	36	12
1.2	283	210	38	248	35	12
1.5	269	200	37	237	32	12
1.8	257	190	36	226	31	12
2.1	244	181	35	216	28	11

Table 2. GENRAY/CQL3D analyses for the simultaneous injection of LH and EC powers as a function of the central radial diffusion coefficient: I_{LH+EC} is the total RF current modeled, including the phase space synergy effect. I_{LH} and I_{EC} is the LH-only and EC-only contributions, respectively. I_{LH}+I_{EC} is the simple of the two. I_{syn} is the synergy current evaluated by subtracting I_{LH}+I_{EC} from I_{LH+EC}.

Figure 9 (a) and (b) display the corresponding model RF power density and current density profiles, respectively, as a function of the central diffusion coefficient. The power density profiles remain centrally peaked, while the power density at ρ = 0.2 ~ 0.4 becomes slightly broadened with the radial transport operator included. Such a broadening can promote phase space interactions in the radial

layer: $0.2 < \rho < 0.4$, which is not the case without the radial transport effect. The current density profile is also notably broadened and smoothed with an inclusion of the radial transport effect even at a small level of $D_0 = 0.3$ m^2/s, as observed in the LHCD-only case in Section 3.1. A centrally peaked but smooth current density profile is salient for both LHCD and ECCD.

Figure 10 compares three RF current density profiles at three different radial diffusion coefficients: D_0 = 0, 0.9, and 2.1 m^2/s. In all cases, the total RF profile, which includes the synergy interaction (blue), exhibits higher current densities than those from the simple sum of the two RF contributions (orange). This higher current density region largely remains inside $\rho \approx 0.2$. However, with an increase in the diffusion coefficient, the current density profile is further broadened while maintaining a maximum current density on-axis. The synergistic current density, as evaluated from the difference between j_{LH+EC} and $j_{LH}+j_{EC,}$ also exhibits a similar characteristic, and the radial layer with a finite level of the synergy currents is extended radially outward to $\rho \approx 0.4$. Note that the LH-driven fast electrons are likely to be impacted more than EC-driven fast electrons from the radial transport effect before slowing down to the thermal range because of their higher velocity.

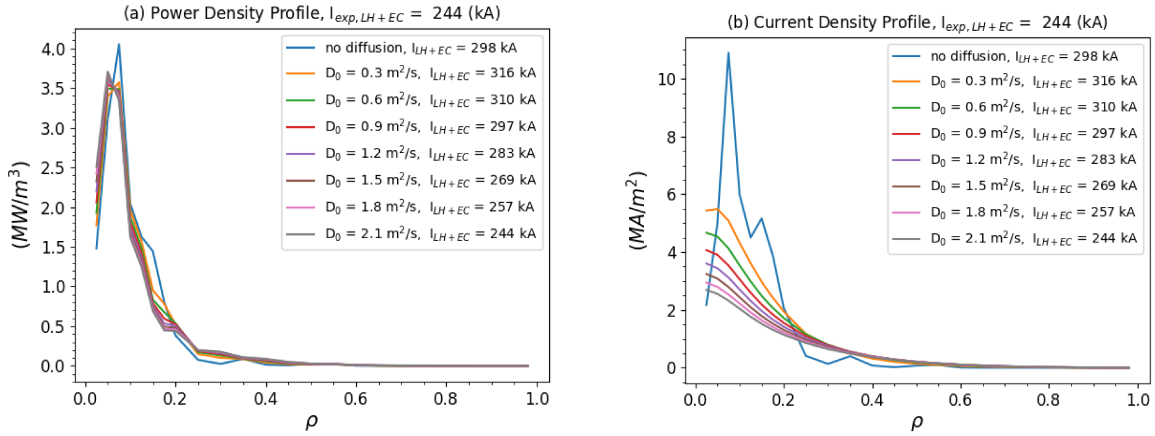

Figure 9. (a) Total RF power deposition and (b) RF current density profiles as a function of the central radial diffusion coefficient for the case of the simultaneous injection of LH and EC powers. The experimental current is 244 kA after subtracting the bootstrap current contribution.

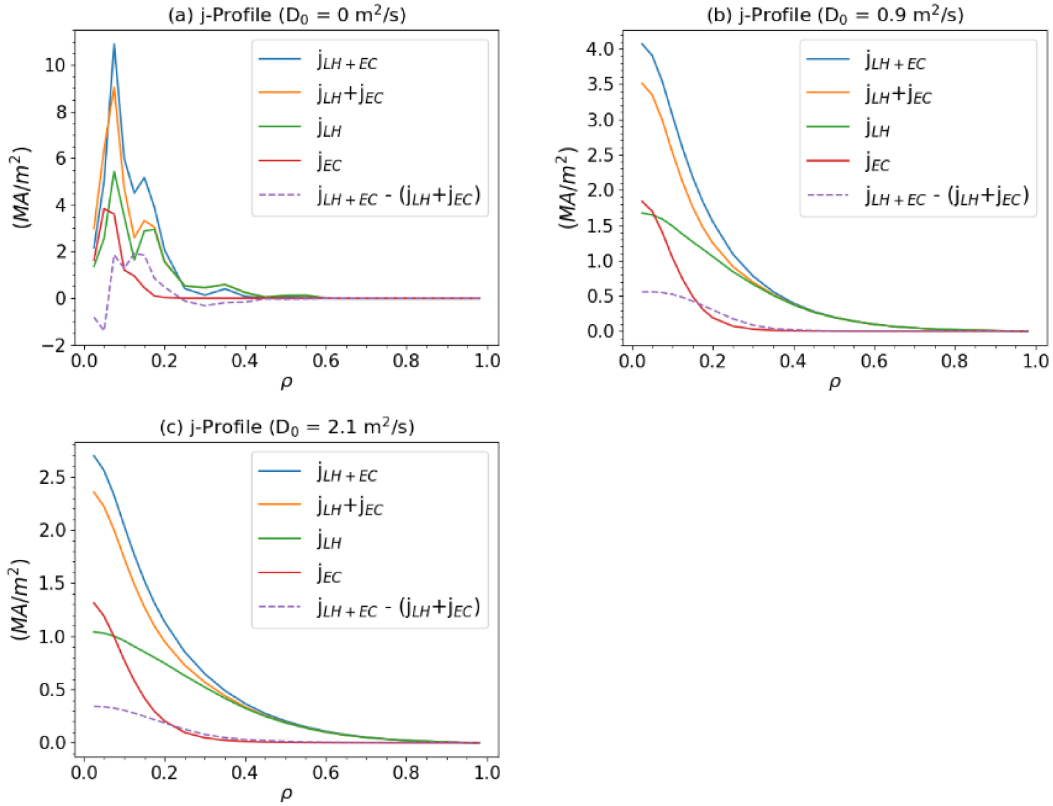

Figure 10. RF current density compositions for (a) D_0 = 0 m²/s, (b) D_0 = 0.9 m²/s, and (c) D_0 = 2.1 m²/s as shown in Table 2: j_{LH+EC} is the total current density that includes the synergy contribution (blue), j_{LH}+j_{EC} is the simple sum of the LH and EC current densities (orange), j_{LH} is the LH current density (green), j_{EC} is the EC current density (red), and the synergy current density j_{LH+EC} – (j_{LH}+j_{EC}) (dashed black)

To illustrate the impact of radial diffusion on synergy current generation, Table 3 and Table 4 compare the local RF current drive efficiency near the on-axis region, ρ = 0.075, for two different diffusion

coefficients of D_0 = 0 m^2/s and 2.1 m^2/s, respectively. First, in the case of D_0 = 0 m^2/s, the total RF power is dominated by the EC power by a factor of three at this flux surface. However, the ECCD efficiency, 0.11 (A/W), is lower by a factor of nearly five compared to the LHCD efficiency, 0.46 (A/W). The addition of the LH power, which is about one-third of the EC power, increases the RF current drive efficiency from 0.11 (A/W) to 0.19 (A/W) when the two current densities are added. When the phase interaction is considered, the synergistic effect increases the RF current drive efficiency by another ~20% from 0.19 (AW) to 0.23 (A/W). Meanwhile, as shown in Table 4, radial transport at D_0 = 2.1 m^2/s reduces the current drive efficiency at this flux surface by one-third for both ECCD and LHCD because current-carrying fast electrons are diffused to neighboring flux surfaces. Nevertheless, the synergy factor (F_{syn}) decreases slightly from 1.5 to 1.3. As shown in Table 2, the total synergy current magnitude remains within the 20 – 36 kA for a range of diffusion coefficients examined, corresponding to ~10% of the total RF current modeled.

ρ = 0.075; D_0 = 0 m^2/s	EC only	LH only	Simple Sum of LH & EC	Simul. LH and EC
RF Power Density (W/cm^3)	2.92	1.0	3.92	4.05
Current density (A/cm^2)	368	556	924	1115
CD efficiency (A/W)	0.11	0.46	0.19	0.23

Table 3: Comparison of model RF power density, flux-surface-averaged current density, and current drive efficiency among the RF sources at ρ = 0.075 of the current profile shown in Figure 10 at D_0 = 0 m^2/s.

ρ = 0.075; D_0 = 2.1 m^2/s	EC only	LH only	Simple Sum of LH & EC	Simul. LH and EC
RF Power Density (W/cm^3)	2.65	0.55	3.2	3.34
Current density (A/cm^2)	102	103	205	237
CD efficiency (A/W)	0.032	0.16	0.05	0.06

Table 4: Comparison of model RF power density, flux-surface-averaged current density, and current drive efficiency among the RF sources at ρ = 0.075 of the current profile shown in Figure 10 at D_0 = 2.1 m^2/s.

To better illustrate the increase in RF current drive efficiency with the synergy interaction, the RF- and the net particle fluxes in the 2D momentum phase space are shown in Figure 11, corresponding to ρ = 0.075 of the RF current profile for D = 0 m^2/s in Figure 10 (a). It is well known that, when combined with the collisional diffusion, LHCD drives the perpendicular flux along the LH resonance band in the momentum space [29] (shaded in blue in Figure 11). The spectral width between $n_{\parallel,1}$ and $n_{\parallel,2}$ is determined by the LH propagation and absorption properties, primarily wave accessibility and Landau damping. The LH resonance condition is determined by the two bounds: $u_{\parallel,1} = \gamma \frac{c}{n_{\parallel,1}}$ and $u_{\parallel,2} = \gamma \frac{c}{n_{\parallel,2}}$, where u is the momentum per rest mass, and γ is the relativistic factor. Meanwhile, ECCD provides a net parallel flux component in conjunction with collisional scattering. The EC resonance band is also defined by the two resonance curves as $u_{\parallel,1} = \gamma \frac{c}{n_{\parallel,1}}(1 - \frac{2\omega_c}{\gamma\omega})$ and $u_{\parallel,2} = \gamma \frac{c}{n_{\parallel,2}}(1 - \frac{2\omega_c}{\gamma\omega})$ for the 2nd harmonic interaction, and is shaded in red in the figure.

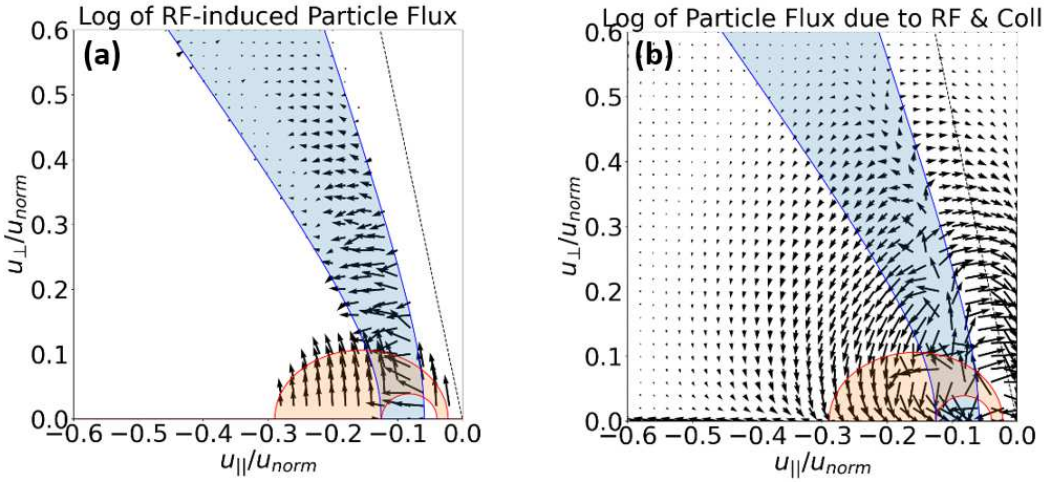

Figure 11. The particle flux vector (a) due to RF only and (b) due to a combination of the RF and collision in the 2D momentum space for the Fokker-Planck analysis at ρ = 0.075 of the RF current profile shown in Figure 10 (a) with D = 0 m^2/s. For visualization, the region shaded in blue (red), corresponding to the LH (EC) resonance region, is overlaid using the two limit values $n_{\|,1}$ and $n_{\|,2}$. The magnitude of the flux vector is a logarithmic value. The negative direction in the parallel momentum space corresponds to the current drive direction. u is the particle momentum per rest mass. u_{norm} is the maximum momentum per rest mass in the simulation domain, corresponding to a kinetic energy of 1 MeV.

A complex pattern of convective cells is observed in the momentum space in Figure 11. ECCD provides a transport channel for the particle flux from a low-energy region into the LH resonance band, which is then channeled into the perpendicular direction into a high-energy space and, finally, pitch-angle scattered out of the LH resonance region. Inspecting the particle flux flow within the ECCD resonance region, one can also see a parallel flow, which will scatter out of the resonance region, splitting into two directions into either lower or higher perpendicular momentum spaces. This combined process of RF quasilinear diffusion, collisional diffusion, and pitch angle scattering in the momentum phase space results in a broadening of the distribution function in the parallel and perpendicular directions in the steady state limit, as shown in the 2D contour plot of the distribution function in Figure 12. The first moment of the distribution function is a net RF-induced current.

Figure 13 shows a 1D cut of the electron distribution function in the current drive direction along the magnetic field at two flux surfaces of ρ = 0.075 and ρ = 0.2 (D_0 = 0 m^2/s). In both locations, there is a clear formation of the plateau created by the LHCD power, as compared to the EC-only case. This plateau's height is higher than that in the LH-only case, showing a source of the synergy current. This is more pronounced at ρ = 0.075, where the EC power density is higher than at ρ = 0.2. Meanwhile, the plateau width is further extended ρ = 0.2 due to a wider spectral width of the LH resonance band. Such build-up in the particle density are due to the particle flux scattered out of the LH and EC resonance bands, ultimately forming a closed interaction system in the momentum space that establishes a steady-state distribution.

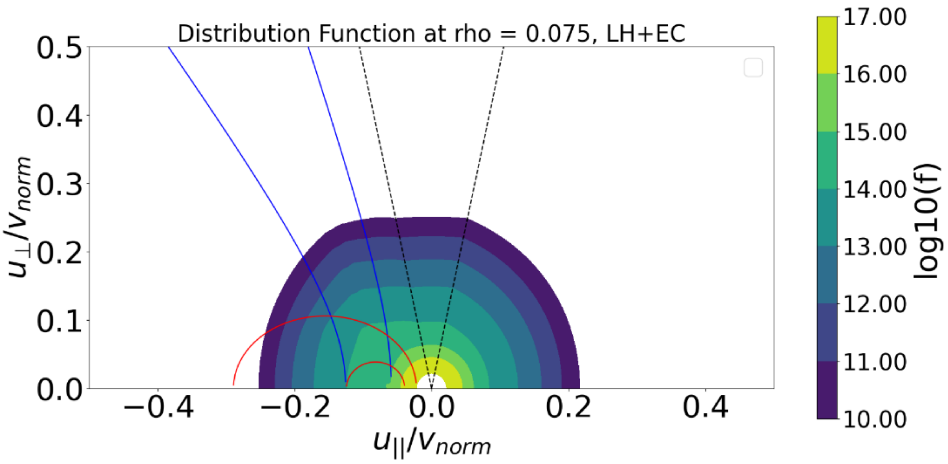

Figure 12: 2D contour plot of the steady-state electron distribution function at ρ = 0.075 of the model profile shown in Figure 10 (D = 0 m^2/s). The two blue (red) curves bound the LH (EC) resonance interaction region in the momentum space.

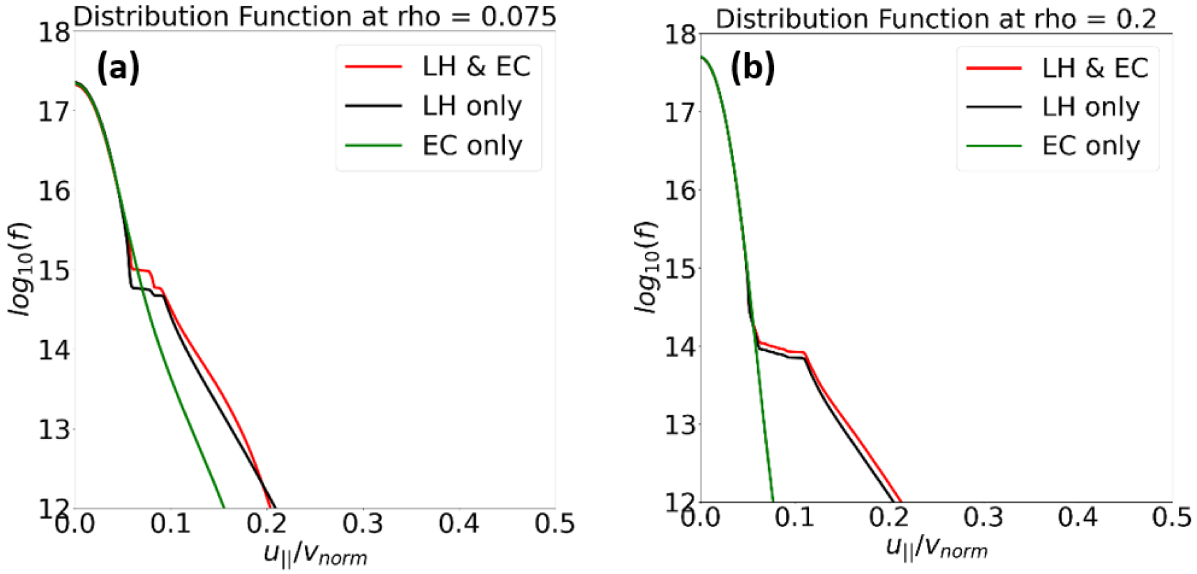

Figure 13: The 1D cut of the electron distribution in the direction of the magnetic field direction. A formation of the raised plateau is observed with both LH and EC at both (left) ρ = 0.075 and (right) ρ = 0.2. See also Table 3.

4. Sensitivity analysis of the LH $k_\perp$-rotation angle on Synergistic Current

Past lower hybrid current drive (LHCD) experiments indicate the important role of interactions between waves and edge/SOL plasmas in determining the magnitude and profiles of LH power deposition. The LH

power losses resulting from collisions [33,34,37], wave scattering by turbulence/blobs [38–40], or parametric decay instabilities (PIs) [18,41–46] are found to be a sensitive function of the edge plasma condition. In particular, wave scattering and parametric instabilities are known to modify the power damping profile by altering the parallel wavenumber spectrum imposed by the antenna. Mitigating parametric instabilities at the edge also correlated with an improved LHCD efficiency at high density ($>1x10^{20}$ m^{-3}) on FTU [47] and Alcator C-Mod [45]. In addition to the LHCD density-limit problem, additional spectral broadening mechanisms are found to be necessary to reproduce LHCD profiles in low- to moderate-density plasmas. Theoretical models point to the importance of additional spectral broadening mechanisms to wave power absorption behaviors [48–50]. For example, parametric instabilities are introduced to explain the experimental LHCD profile on JET [51], specifically to interpret the off-axis current drive profile. Without the spectral modification induced by PIs, the central power deposition is predicted, which was inconsistent with the experimental q-profile measured.

While potentially non-negligible, the impact of PIs is likely to be minimal for the discharge of interest for the following two reasons. First, the plasma condition considered here (low density below $2x10^{19}$ m^{-3} and high source frequency at 4.6 GHz) is expected to mitigate or suppress parametric instabilities, as supported by the frequency spectral measurements [19]. Pump broadening is minimized, and the ion cyclotron sideband is suppressed at this low density. Second, the plasma discharge #106915, whose density and temperature profiles are adopted for our analysis of #106904 in Section 2, exhibits a monotonous q-profile [22], indicating central power deposition without clear evidence of off-axis current drive, as analyzed on JET [51]. Therefore, the low-density, high-temperature conditions likely suppressed the impact of PIs in the target discharge.

Wave scattering is another wave-edge interaction that could potentially be important. It was introduced to interpret the central power deposition observed on Tore Supra [52] and Alcator C-Mod [40,53]. The standard ray tracing model often predicts off-axis power damping with an inherent toroidal/poloidal up-shift mechanism in the multi-pass damping regime. Such a wave damping profile in a multi-pass damping regime is also reproduced in a full wave model, suggesting that full wave effects—such as diffraction and interference—play a minor role even in the Alcator C-Mod multi-pass damping regime [54]. It is important to note that the geometric optics approximation can break down, particularly at the plasma edge boundary cut-off layers and ray caustics, and discrepancies between the full-wave and ray-tracing models have been reported [55,56]. Wave scattering may provide a spectral component promoting on-axis power damping on the first pass. On EAST, a heuristic approach was applied in ray-tracing/Fokker-Planck analysis by introducing an ad-hoc rotation angle to the initial LH perpendicular wavevector to identify an optimal scattering angle that best fits the experimental profile across the density range [57]. This section adopts a similar approach to examine the impact of LH wave scattering on synergistic current generation. Unlike the previous EAST analysis, this study considers a high central temperature plasma, resulting in a high level of LHCD absorption on the first pass.

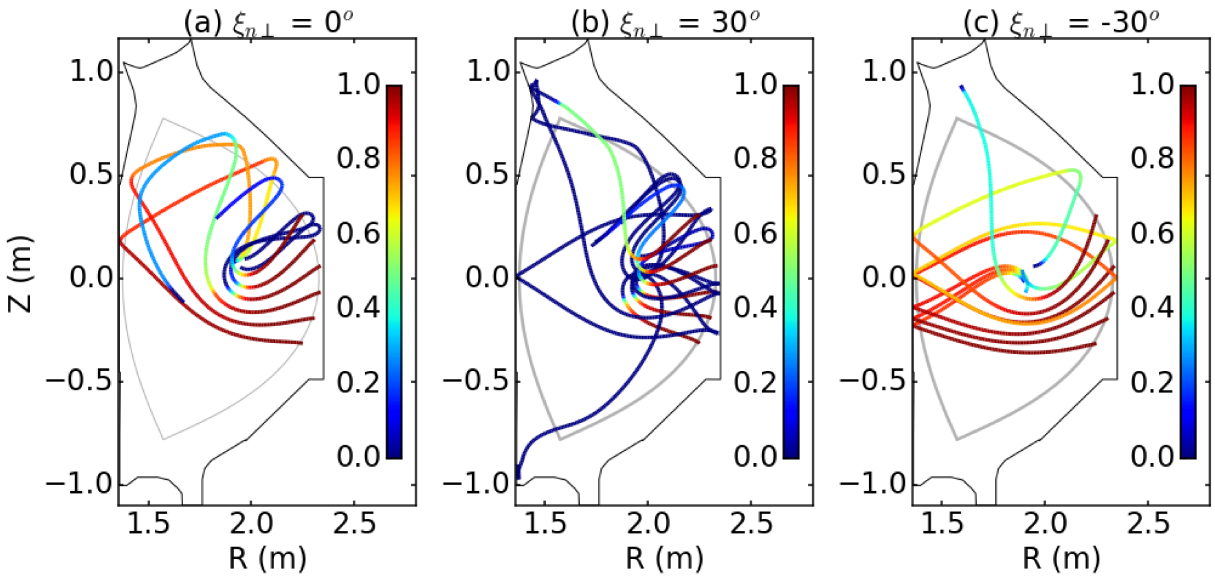

Figure 14.Five LH ray trajectories with (a) $\xi_{n\perp}$= 0°, (b) $\xi_{n\perp}$= 30°, and (c) $\xi_{n\perp}$= -30°. The color denotes the normalized ray power.

A standard treatment in a ray-tracing approach is to align the initial LH perpendicular wavevector to the normal direction of the flux surface, $\hat{e}_{\nabla\psi}$, as in the experiments using the grill antenna, which has a geometrical contour matching the plasma shape. However, it is known that wave scattering by drift-wave-type or filamentary density fluctuations in the edge/SOL region can interact with lower hybrid waves, rotating the perpendicular wavevector in the 2D perpendicular space based on the three-wave matching condition [39]. This rotation allows the lower hybrid perpendicular wavevector to acquire finite toroidal and poloidal components as follows:

$$\vec{k}_\perp = k_\perp \cos\xi_{n\perp}\,\hat{e}_{\nabla\psi} - k_\perp \sin\xi_{n\perp}\left(\hat{e}_\varphi \frac{B_\theta}{B} - \hat{e}_\theta \frac{B_\varphi}{B}\right)$$

where $\xi_{n\perp}$ is the angle between the lower hybrid perpendicular vector $\vec{k}_\perp$ and the unit vector normal to the flux surface $\hat{e}_{\nabla\psi}$. In the absence of wave scattering, $\xi_{n\perp}$= 0 and the second and third terms, which contain the poloidal and toroidal components, are zero. However, a finite magnitude of toroidal and poloidal components can affect the wave propagation and absorption profiles significantly as the wave parallel refractive index $n_{||}$ up-shift mechanism depends on interaction with the local magnetic field and its shear as the following:

$$n_\parallel = \vec{n}\cdot\frac{\vec{B}}{|\vec{B}|} = \frac{n_\varphi \cdot B_\varphi + n_\theta \cdot B_\theta}{\mathrm{B}} \approx n_\varphi \frac{B_\varphi}{\mathrm{B}} + n_\theta \frac{r}{R_0}\frac{1}{q}$$

where $\mathrm{q} = \frac{r}{R_0}\frac{B_\varphi}{B_\theta}$ is the safety factor. Figure 14 shows an example of ray trajectories at three different rotation angles at the initial launch point. A positive rotation angle, for example, at $\xi_{n\perp}$ = 30° provides a stronger $n_{||}$ up-shift on the first pass than the reference case at $\xi_{n\perp}$ = 0°. The positive (negative) sign indicates that the perpendicular wavevector has a component that is parallel (anti-parallel) to the local poloidal magnetic field at the initial position. Wave scattering can introduce these finite k_θ components,

providing wave components that can produce central power absorption even in a weak single-pass plasma. In contrast, with a negative rotation angle (e.g., $\xi_{n\perp}$ = - 30° in Figure 14 (c)), the wave acquires more of the toroidal component, while the initial poloidal component is further reduced. While the toroidal effect (~1/R) plays a role, its impact on $n_{||}$ up-shift is generally weaker than the poloidal effect. Radial penetration is reduced, as seen by the ray trajectory in Figure 14 (c). Nevertheless, because of a high central temperature in the target plasma, on-axis power damping occurs on the second pass after a reflection at the high-field-side of the plasma. This ray propagation and absorption behavior is notably different from that in a multi-pass damping regime with a low central temperature (~ 2 keV), which typically requires several passes before waves are up-shifted enough for Landau absorption because of a strong dependence on the wave poloidal mode number. In the previous EAST study, an effective scattering angle in the range of $\xi_{n\perp}$ = 20° - 40° was seen to best reproduce the experimental profile.

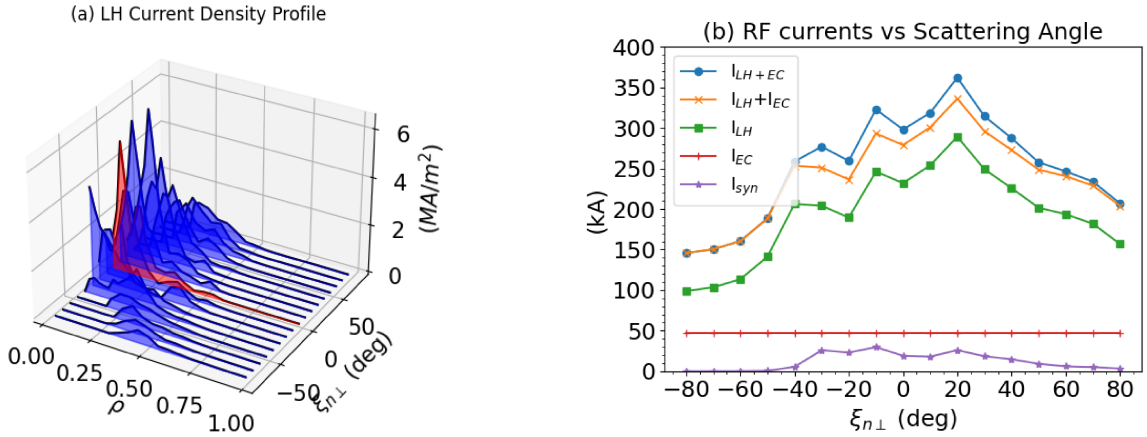

Figure 15. (a) LH current density profiles as a function of $\xi_{n\perp}$. The current density profile at $\xi_{n\perp}$= 0° is a profile with a red-shaded region. (b) RF currents as a function of $\xi_{n\perp}$, including the total (I_{LH+EC}), simple sum (I_{LH}+I_{EC}), LH current (I_{LH}), EC (I_{EC}), and the synergy current (I_{syn}).

Figure 15 (a) shows the variation in LH current density profiles as a function of $\xi_{n\perp}$. No radial transport is considered. Power deposition remains to the inner half of the plasma ρ < 0.5 due to a high central temperature, even at a large scattering angle imposed. Unlike in low- to moderate-temperature plasma, a high temperature in the on-axis region provides a target for Landau damping within a few passes. The profile is peaked in the central region except at a larger negative angle (e.g., $\xi_{n\perp}$ < -50°). Figure 15 (b) displays the modeled RF currents as a function of $\xi_{n\perp}$, including the total current (I_{LH+EC}), the simple sum of the LH and EC currents (I_{LH}+I_{EC}), the LH current (I_{LH}), the EC (I_{EC}), and the synergy current (I_{syn}). The synergy current is evaluated by subtracting the simple sum of the LH and EC currents (I_{LH}+I_{EC}) from the total current (I_{LH+EC}). In this scan, I_{EC} remains constant as no angular rotation is assumed. I_{syn} is finite and significant in the angular range of -40° < $\xi_{n\perp}$ < 40° where LH power deposition overlaps with the EC power deposition at ρ < 0.2. Compared to the reference case at $\xi_{n\perp}$ = 0°, introducing a scattering angle in a moderate range continues to generate synergy currents of a similar magnitude (20 ~ 30 kA range). If the scattering angle is largely negative ($\xi_{n\perp}$ < -40°), the LH deposition radially shifts outward (ρ > 0.25), resulting in no significant level of spatial overlapping between the LH and EC power depositions and a negligible level of the synergistic currents.

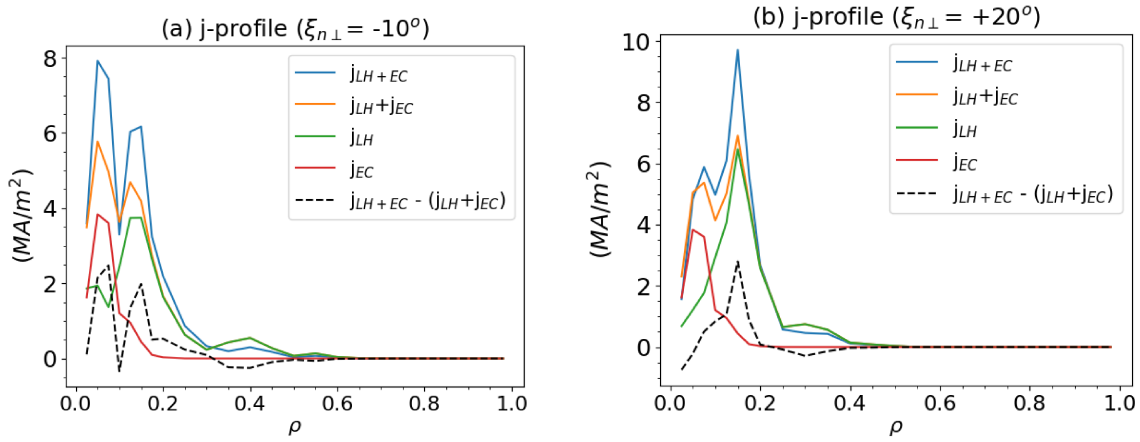

Figure 16. RF current profiles (a) at $\xi_{n\perp}$= -10° and (b) at $\xi_{n\perp}$= +20°. j_{LH+EC} is the total current density that includes the synergy contribution (blue), j_{LH}+j_{EC} is the simple sum of the LH and EC current densities (orange), j_{LH} is the LH current density (green), j_{EC} is the EC current density (red), and j_{LH+EC} – (j_{LH}+j_{EC}) is the synergistic current (dashed black).

Figure 16 shows two RF current density profiles at $\xi_{n\perp}$ = -10° (the scattering angle that generates the highest level of the synergy current of 28 kA) and $\xi_{n\perp}$ = +20° (the scattering angle that generates the highest level of the LH current of 334 kA and the corresponding synergy current of 24 kA). The reference profile at $\xi_{n\perp}$ = 0° is shown in Figure 10 (a) above. At $\xi_{n\perp}$ = -10°, the LH current density remains above 2 MA/m^2 on-axis, providing sufficient LH-driven fast electrons for a synergistic interaction with the EC power at ρ = 0.05, where the EC current density is the highest. With a positive angle of $\xi_{n\perp}$ = +20° in Figure 16 (b), however, the peak of the LH current density profile is shifted radially outward to ρ ≈ 0.15, resulting in a mismatch with the ECCD peak current density location. However, this location coincides with the peak location of the synergy current generated (black dashed), while the EC power density is not as high as that on-axis. This aspect will be discussed more in the power scan below in Section 5. Also, the total current density profile (in blue), as resulting from the combined RF effects, generates a more radially peaked profile than the simple sum of the two LH and EC profiles (in orange), suggesting the importance of considering a self-consistent phase space interaction in the current drive calculation.

The impact of radial transport in the presence of the scattering effect is evaluated. Figure 17 (a) shows the LH current density profiles as a function of $\xi_{n\perp}$ with a central radial transport coefficient of D_0 = 2.1 m^2/s. This level of radial diffusion quantitatively matched the experimental current, as discussed in Table 2 above. Compared to Figure 15 (a), the inclusion of the radial transport effect eliminates the jaggedness arising from the local power deposition, resulting in a generally smooth, centrally peaked profile, regardless of the scattering angle imposed. The maximum on-axis LH current density is ~1.5 MA/m^2 at $\xi_{n\perp}$ = 20°. This is also the scattering angle at which the LH current is maximized to 250 kA (orange), as shown in Figure 17 (b). This figure also illustrates that the synergistic current remains in the range of 10 - 30 kA across a wide range of scattering angles of -30° < $\xi_{n\perp}$ < +60°. This synergy current fraction again accounts for approximately 3 – 12 % of the total RF current. Previous studies found an optimal scattering angle for the EAST plasmas in the multi-pass damping regime to be in the range of $\xi_{n\perp}$ = 20° to 40° for best matching of the profile shape. In this study, this angular range also reproduces the

experimental RF currents (~244 kA) within 10% after incorporating radial transport. A measurement of internal current density profile will be needed in future experiments.

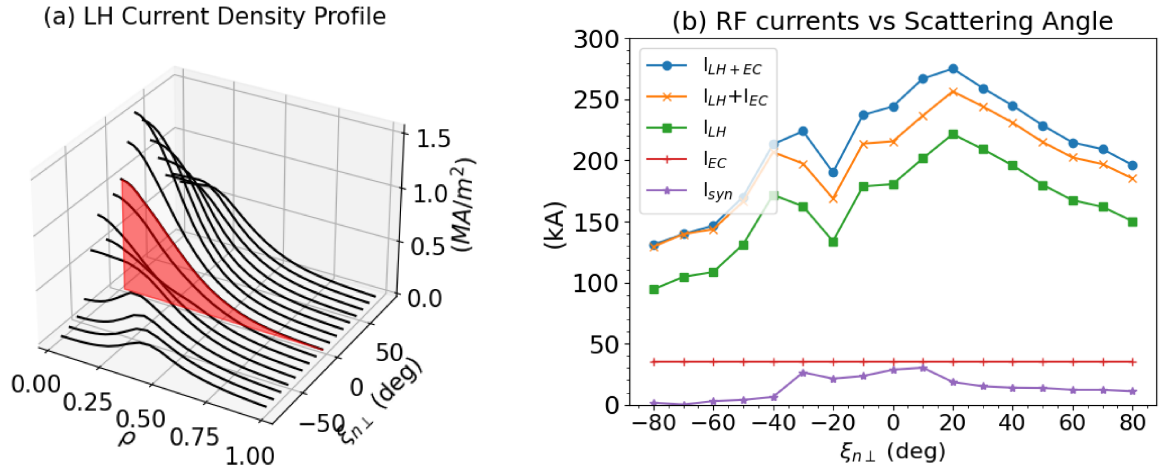

Figure 17. (a) LH current density profiles as a function of $\xi_{n\perp}$ with a radial transport effect included (D_0 = 2.1 m^2/s). The current density profile at $\xi_{n\perp}$= 0° is a profile with a red-shaded region. (b) RF currents as a function of $\xi_{n\perp}$, including the total (I_{LH+EC}), simple sum (I_{LH}+I_{EC}), LH current (I_{LH}), EC (I_{EC}), and the synergy current (I_{syn}).

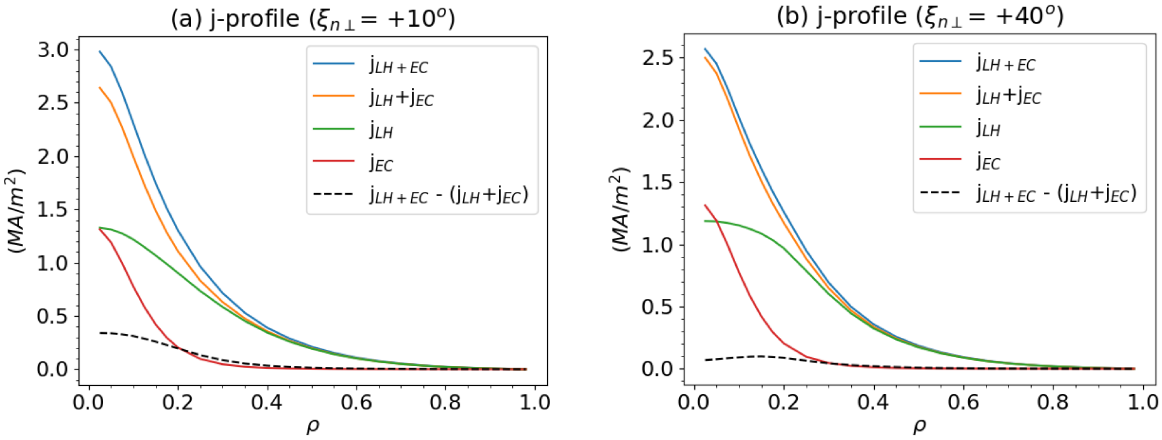

Figure 18. RF current profiles (a) at $\xi_{n\perp}$= +10° and (b) at $\xi_{n\perp}$= +40° with the central diffusion coefficient of D_0 = 2.1 m^2/s. j_{LH+EC} is the total current density that includes the synergy contribution (blue), j_{LH}+j_{EC} is the simple sum of the LH and EC current densities (orange), j_{LH} is the LH current density (green), j_{EC} is the EC current density (red), and $j_{LH+EC} - (j_{LH}+j_{EC})$ is the synergistic current (dashed black).

To examine the radial profile of synergy current generation across the scattering angle, Figure 18 shows two RF current density profiles at $\xi_{n\perp} = +10°$ (which generates a maximum synergy current of 30 kA) and $\xi_{n\perp} = +40°$ (which generates a total current of 245 kA that also best matches the experimental RF current, in addition to the reference case at $\xi_{n\perp} = 0°$). In the $\xi_{n\perp} = +40°$ case, the total synergistic current predicted is only 14 kA vs. 28 kA at $\xi_{n\perp} = 0°$, showing a sensitivity of synergy current magnitude to the scattering angle.

Figure 18 also shows that the on-axis synergy current density at ρ = 0.025 differs significantly between the two cases (0.35 MA/m^2 in the $\xi_{n\perp} = +10°$ case vs. 0.07 MA/m^2 in the $\xi_{n\perp} = +40°$ case), despite the similar LH current densities of 1.33 and 1.19 MA/m^2, respectively. The LH power densities, however, differ significantly because not a substantial amount of LH power is deposited in the on-axis region in the $\xi_{n\perp} = +40°$ case; the peak power deposition region shifts radially outward to ρ ≈ 0.2 at this high scattering angle. The LH currents at ρ = 0.025 result almost entirely from fast electrons that are spatially diffused radially inward. Such a weak LH drive is seen in the magnitude of the RF quasilinear diffusion coefficient. Figure 19 shows the RF quasilinear diffusion coefficient in the 2D momentum space between $\xi_{n\perp} = +10°$ and $\xi_{n\perp} = +40°$. In the latter, the spectral coverage of the LH resonance band in momentum space shifts toward a higher energy range, and its width is notably reduced due to the limited LH spectral range absorbed. Furthermore, the magnitude of the LH quasilinear diffusion coefficient is lower by five orders of magnitude due to the lack of the LH power itself. As shown by the synergy current density profile in Figure 18 (b) above, most of the synergistic interaction occurs at ρ ≈ 0.15 where the EC drive is weak, thus resulting in a low level of the synergy current.

As a section summary, the LH wave $\xi_{n\perp}$ angular scan shows that the magnitude of the synergistic current generation remains comparable to the no-scattering case within a scattering angle range that reproduces the experimental current magnitude. The strong interaction region still persists in the on-axis region, which ensures the co-damping of LH and EC powers due to high central temperature, while its profile can be diffused in space up to ρ ≈ 0.4, particularly with the inclusion of fast-electron radial transport.

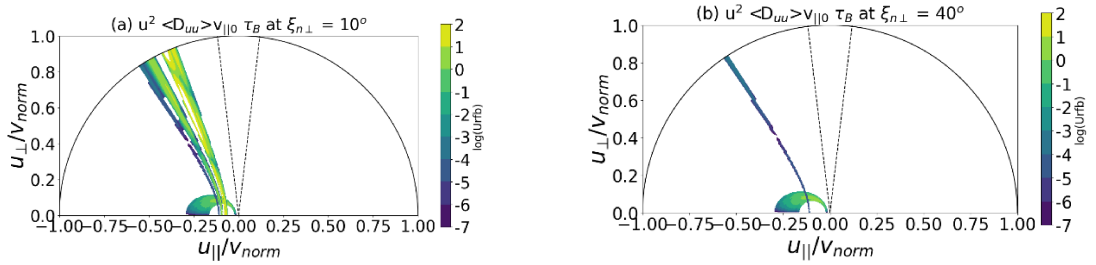

Figure 19. Normalized RF quasilinear diffusion coefficient for the flux surface at ρ = 0.025 for (a) $\xi_{n\perp}$= +10° and (b) $\xi_{n\perp}$= +40°. Please see Figure 18 for the current density profiles. v_{norm} is the maximum momentum per rest mass in the simulation domain, corresponding to a kinetic energy of 1 MeV.

5. Sensitivity Analysis of the EC injection angle on Synergistic Current

This section examines the sensitivity of the synergy current to the ECCD injection angles. For the scenario analyzed above, a question arises as to whether the synergistic current can be increased further by modifying the ECCD deposition characteristics in either the spatial or momentum space. To investigate this, the ECCD toroidal and poloidal injection angles are numerically varied by stepping each injection angle by 2 degrees at a fixed EC power of 495 kW. Generic density and temperature profiles are used. Refer to Figure 2 for the definition of the EC toroidal injection angle (α) and poloidal injection angle (β). In the scan, α (β) is varied from 180° (60°) to 220° (90°). The LH power is held constant at 540 kW. Only the primary peak $n_{||}$ component is considered in this scan, and fast-electron radial transport is

neglected. Figure 20 shows the sensitivity of EC power deposition and ray $n_{||}$ evolutions as a function of α and β. It illustrates that the toroidal injection angle (α) strongly impacts the wave $n_{||}$ and, therefore, the power deposition radius. Variation in the poloidal injection angle (β) also influences the power deposition location but has a weaker effect on wave $n_{||}$ than the toroidal injection angle.

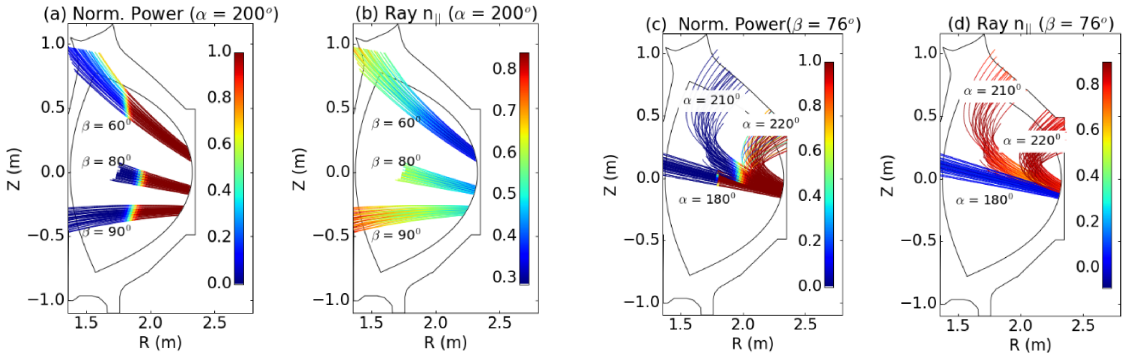

Figure 20. (a) The normalized EC ray power and (b) the wave $n_{||}$ as a function of the ray trajectories at three different poloidal injection angles of β = 60°, 80°, and 90° at the fixed toroidal injection angle α = 200°. (c) The normalized EC ray power and (d) the wave $n_{||}$ as a function of the ray trajectories at two different toroidal injection angles of α = 180°, 210°, and 220° at the fixed poloidal injection angle β = 76°. If the EC ray hits the wall boundary, the rays are terminated, and the remaining ray power is assumed to be lost.

Figure 21 shows 2D tile plots of the resulting the synergy current $I_{syn} = I_{LH+EC} - (I_{LH}+I_{EC})$ and the corresponding synergy factor F_{syn} as a function of poloidal and toroidal injection angles. It is seen that both the synergy current and synergy factor show a greater dependence on the toroidal injection angle. The synergy factor can increase to approximately 3.5 at high toroidal injection angles. The synergy current varies from around 5 to 38 kA in this parameter set. The maximum total RF current is approximately 250 kA, with the synergy current contributing around 15%. As a reference, the experimental condition in Section 2 corresponds to α = 200° and β = 77°, with $F_{syn} \approx 1.3$. The stronger dependence of F_{syn} on the toroidal injection angle suggests that the phase space overlapping also plays an important role, in addition to physical overlapping.

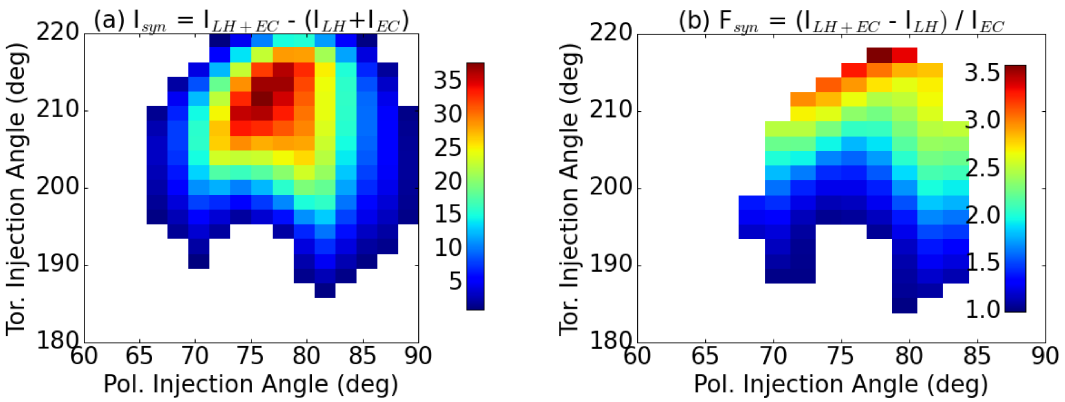

Figure 21. 2D tile plot of (a) the synergy current, I_{syn} = $I_{LH+EC} - (I_{LH} + I_{EC})$, in kA and (b) the synergy current factor, F_{syn} = $(I_{LH+EC} - I_{LH}) / I_{EC}$ as a function of the poloidal and toroidal injection angles. Both the LHCD and ECCD power are constant.

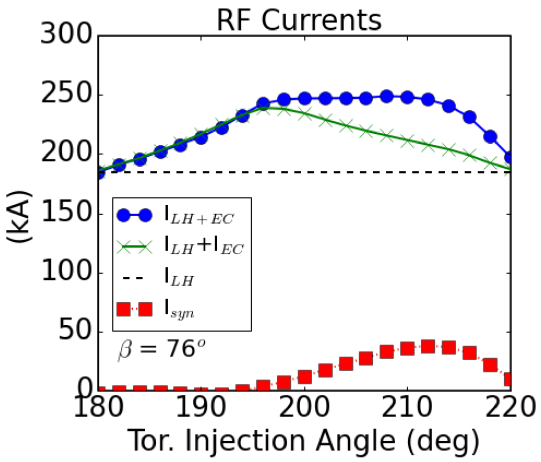

Figure 22. RF currents predicted as a function of the ECCD toroidal injection angle at a constant ECCD poloidal injection angle at 76 degrees: I_{LH+EC} is the total LH and EC current that includes the synergy current (blue circle), I_{LH}+I_{EC} is the simple sum of the two contributions (green cross), I_{LH} is the LH contribution (black dash), and I_{syn} = $I_{LH+EC} - (I_{LH}+I_{EC})$ is the synergistic current arising from the phase space interaction between the LH and EC waves.

To further examine the toroidal angle dependence, Figure 22 shows the RF currents as a function of the toroidal injection angle, α, with a fixed poloidal injection angle at β = 76°. The case with α = 180° corresponds to pure EC heating. The total RF current (in blue circle), I_{LH+EC}, which includes the synergy current contribution, increases with α up to α = 200°. However, no appreciable synergy contribution is evaluated in this range, as indicated by its overlap with the simple sum case (in green x), $I_{LH} + I_{EC}$. As shown in Figure 23, the EC current density (in red square), and correspondingly the power density, shifts radially inward from ρ ≈ 0.1 at α = 190° to ρ ≈ 0 at α = 200°, then shifts outward back to ρ ≈ 0.15 at α = 210°. Although the ECCD current itself starts to decrease at α > 200°, the synergistic effect begins to appear in the α range between 200° and 210°, as shown by the constant level of the total RF current I_{LH+EC} (in blue circle). ECCD efficiency decreases for α > 200° because of the trapping effect. However, it is

compensated by the synergy current up to α ≈ 210°, a feature that may offer scenario flexibility in future experiments.

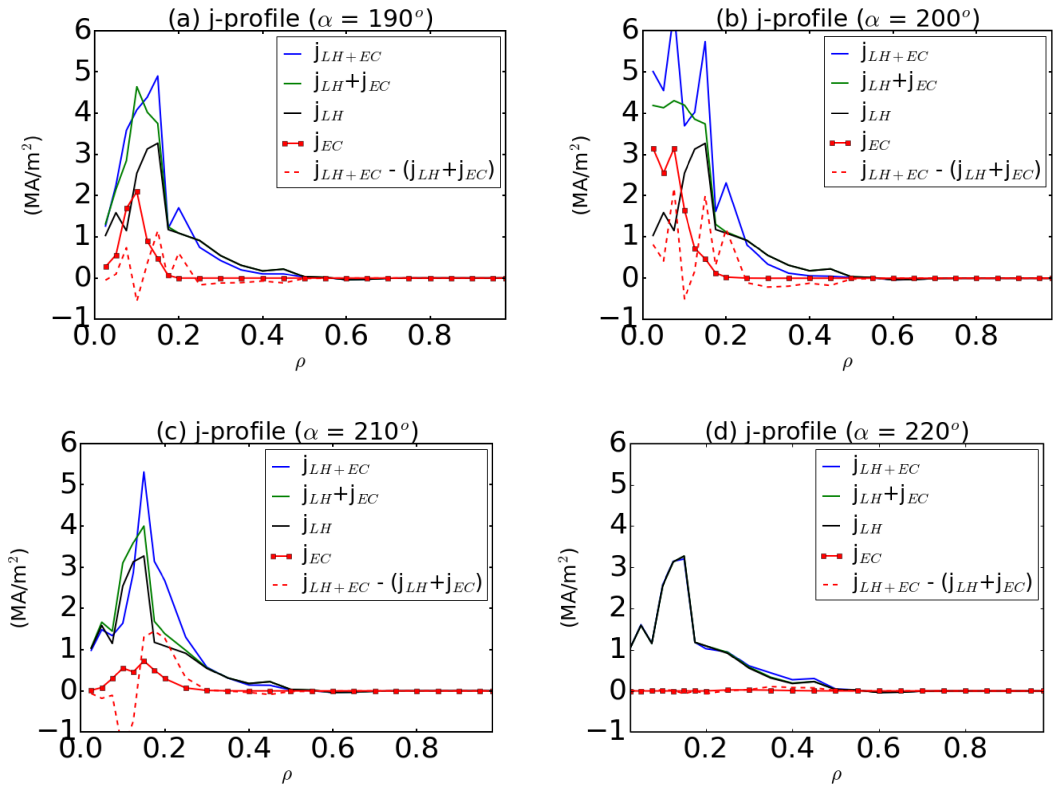

Figure 23: RF current density profiles at the toroidal injection angle of (a) α = 190°, (b) α = 200°, (c) α = 210°, and (d) α = 220°. The poloidal injection angle (β) is fixed at 76°. j_{LH+EC} is the total LH and EC current density that includes the synergy current (blue), j_{LH}+j_{EC} is the simple sum of the two contributions (green), j_{LH} is the LH contribution (black), j_{EC} is the EC contribution (red dot), and $j_{LH+EC} - (j_{LH}+j_{EC})$ (red dash) is the difference between the two, representative of the synergistic current.

The following analyzes the impact of on-axis (ρ ≈ 0) vs. off-axis (ρ ≈ 0.15) ECCD on synergy interaction while keeping the LH contribution fixed. First, Figure 23 (b) displays a model RF current density profile for α = 200° and β = 76°, corresponding to the nominal experimental condition, resulting in on-axis ECCD. A centrally peaked profile is evident for both LHCD and ECCD. The total RF profile, which includes the synergistic interaction (blue), exhibits higher current densities than those from the simple sum of the two RF contributions (green). This higher current density is inside the normalized radial radius of ρ < 0.15. Figure 23 (c) displays a model RF current density profile with off-axis ECCD at ρ = 0.2 with α = 210° and β = 76°, corresponding to the near maximal generation of synergy current of I_{syn} = 34 kA. This current exceeds the EC contribution at I_{EC} = 27 kA, resulting in a synergy factor of F_{syn} = 2.2. The resulting current profile (in blue) exhibits an increased level of current density in the radial range between ρ = 0.15 and ρ = 0.3, compared to the simple sum case (in green). Inside ρ = 0.15, the current density is lower than the simple sum case, indicating a more localized power damping profile, as indicated by the difference between j_{LH+EC} and j_{LH}+j_{EC}, indicating that the resulting deposition profile is modified with a

combined RF quasilinear diffusion coefficient. The localized peak in the current density profile at $\rho \approx 0.2$ coincides with the maximal difference between j_{LH+EC} and $j_{LH}+j_{EC}$.

Table 5 compares the RF current drive efficiency at the on-axis location, $\rho = 0.075$. At this flux surface, the total RF power is dominated by the EC power by a factor of ten, but the ECCD efficiency, 0.10 (A/W), is lower by a factor of five than the LHCD efficiency, 0.46 (A/W). The synergy interaction increases the total current drive efficiency from 0.13 (AW) to 0.18 (A/W) by 40%.

$\rho = 0.075$; Figure 23 (b).	EC only	LH only	Simple Sum of LH & EC	Simul. LH and EC
RF Power Density (W/cm^3)	2.69	0.21	2.90	3.13
Current density (A/cm^2)	322	118	440	665
CD efficiency (A/W)	0.10	0.46	0.13	0.18

Table 5. Comparison of model RF power density, flux-surface-averaged current density, and current drive efficiency among the RF sources at $\rho = 0.075$ of the current profile shown in Figure 23 (b). At this radial location, the RF power is dominated by the EC power by a factor 10.

Table 6 shows the corresponding ECCD efficiency at the flux surface of $\rho = 0.2$. Its efficiency is reduced by about half to 0.056 (A/W) from 0.1 (A/W) at $\rho = 0.075$ in Table 5 due to its power damping at a radially outward flux surface. The LHCD efficiency remains similar because it is less affected by the trapping effect. With the concurrent presence of LH and EC, the RF current drive efficiency increases by 47% from 0.19 (A/W) to 0.28 (A/W), as shown in the last row in the table. When applying Fidone's rule of thumb at this flux surface, $F_{syn} = (j_{LH+EC} - j_{LH})/j_{EC} = 5.29$, which is three times higher than the on-axis case in Table 5, despite the EC power density being lower by a factor of 5 and the ECCD efficiency itself being about half as high. This high F_{syn} value suggests that off-axis synergy between LHCD and ECCD could be particularly advantageous, as the combined effect on current generation is maximized while ECCD efficiency decreases off-axis.

$\rho = 0.2$; Figure 23 (c)	EC only	LH only	Simple Sum of LH & EC	Simul. LH and EC
RF Power Density (W/cm^3)	0.47	0.20	0.67	0.85
Current density (A/cm^2)	31.7	116	147.7	284
CD efficiency (A/W)	0.056	0.5	0.19	0.28

Table 6. Comparison of RF power density, current density, and current drive efficiency among the RF sources at $\rho = 0.2$ for a model case shown in Figure 23 (c). At this radial location, the RF power is dominated by the EC power by a factor of about 2.5.

Figure 24 compares the RF quasilinear diffusion coefficient contour plot between the two cases. The RF particle flux vectors are overlaid as well. In the latter case of off-axis ECCD with a peak synergy current density at $\rho \approx 0.2$, the EC resonance region and its quasilinear diffusion coefficient are larger by an order of magnitude than the on-axis ECCD case ($\rho = 0.075$). The spectral overlap of the EC resonance to the LH resonance strip is also improved in the sense that the LH quasilinear diffusion coefficient is greater at this flux surface ($\rho = 0.2$) and occupies a wider range of $n_{||}$-space, enhancing synergistic interaction. Figure 24 (b) clearly shows that RF-driven particle fluxes possess both the parallel and perpendicular components in the overlapping region, which would create fast electrons carrying high energy and momentum, improving total current drive efficiency.

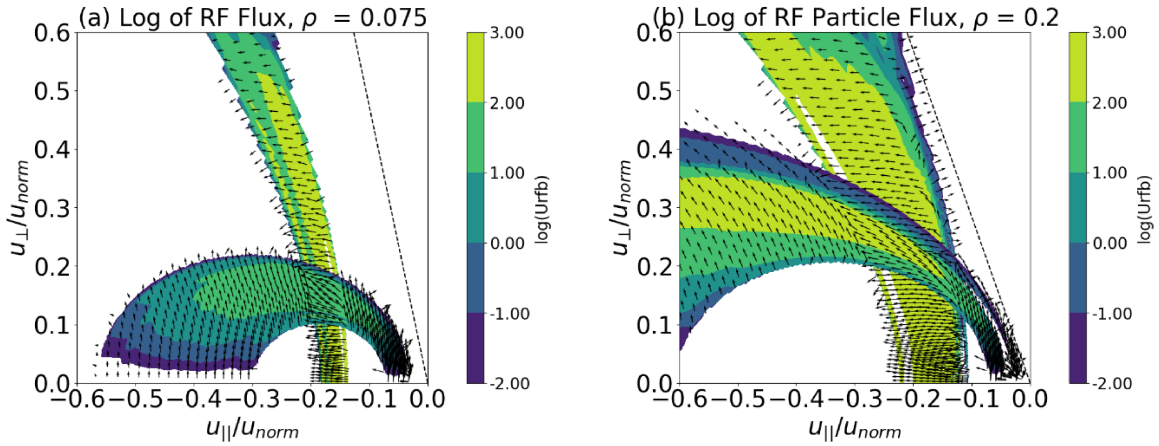

Figure 24. Normalized RF quasilinear diffusion coefficient (Urfb) for the flux surface: (a) at ρ = 0.075 for the case shown in Table 5 (toroidal injection angle = 200°, poloidal injection angle = 76°) and (b) at ρ = 0.2 for the case shown in Table 6 (toroidal injection angle = 210°, poloidal injection angle = 76°). The color bar denotes the logarithm of the RF diffusion coefficient. The overlaid vector plots represent the RF particle flux on a logarithm scale.

The numerical observation that F_{syn} can be larger even when ECCD power itself is lower suggests that ECCD power level itself is not the sole determining factor, motivating further characterization of the roles of LHCD and ECCD power in synergy generation. To evaluate wave power dependence of the synergistic current fraction, the input EC and LH powers are numerically scanned for the case of maximal synergistic current generation (α = 210° and β = 76°), as discussed in Figure 23 (c) and Figure 24 (b). Table 7 and Table 8 show the variation of the synergy current fraction (I_{syn} / I_{LH+EC}) and the corresponding synergy factor (F_{syn}) at four different EC and LH powers, respectively. In both tables, the first row is the reference case examined above, and in the remaining three cases, the EC (LH) power is raised up to nearly five times the reference value. For the ECCD power scan, the synergistic current fraction increases from 15% to 33%, while F_{syn} decreases slightly from 2.3 to 2.0.

Interestingly, an opposite trend is seen in the LHCD power scan. The synergy current fraction decreases from 15% to 9% with an increase in the LHCD power, while F_{syn} increases from 2.3 to 5.1. Such a dependence can be understood by inspecting the 1D cut of the electron distribution functions at different input powers, as shown in Figure 25. As compared to the reference case at P_{LH} = 0.5 MW, a higher LH power is further flattening the plateau. Increasing the LHCD power alone does not further raise the height of the plateau at the lower limit (Landau damping), while it can saturate the plateau to the upper limit (accessibility). As P_{LH} increases, the current drive becomes dominated by LHCD, which reduces the fraction of the synergistic current (I_{syn}/I_{LH+EC}) for the fixed ECCD power. However, the synergy factor (F_{syn}) increases because a higher P_{LH} provides a further momentum/energy input for the particles provided by ECCD.

On the other hand, increasing P_{EC} from 0.5 MW to 2.2 MW raises the plateau height by providing more resonant particles into the LH resonance region. The ECCD quasi-linear diffusion coefficient is increased correspondingly. As a result, the synergy current fraction to the total RF current also increases with an increase in ECCD power. In contrast, the synergy factor remains nearly the same due to the

simultaneous increase in its own ECCD contribution. The analysis implies that optimal synergy generation may not necessarily correspond to the highest power levels of two input powers. Instead, an optimal combination would depend on the specific scenario considered (e.g., maximizing the synergy current fraction or the synergy factor).

P_{EC} (MW)	I_{LH+EC} (kA)	I_{LH} (kA)	I_{EC} (kA)	I_{syn} (kA)	I_{syn} / I_{LH+EC}	F_{syn}
0.49	247	184	27	36	0.15	2.3
1.1	343		71	88	0.26	2.2
1.65	443		123	136	0.31	2.1
2.2	555		187	184	0.33	2.0

Table 7. Synergistic current (I_{syn}) and synergy factor (F_{syn}) as a function of the EC power (P_{EC}). The LH power is fixed at 0.5 MW. The wave and plasma parameters correspond to the maximal synergistic current generation case with the toroidal injection angle = 210° and the poloidal injection angle = 76°.

P_{LH} (MW)	I_{LH+EC} (kA)	I_{LH} (kA)	I_{EC} (kA)	I_{syn} (kA)	I_{syn} / I_{LH+EC}	F_{syn}
0.5	247	184	27	36	0.15	2.3
1.35	625	522		76	0.12	3.8
2.02	905	781		97	0.11	4.6
2.66	1180	1042		112	0.09	5.1

Table 8. Synergistic current (I_{syn}) and synergy factor (F_{syn}) as a function of the LH power (P_{LH}). The EC power is fixed at 0.49 MW. The wave and plasma parameters correspond to the maximal synergistic current generation case with the toroidal injection angle = 210° and the poloidal injection angle = 76°.

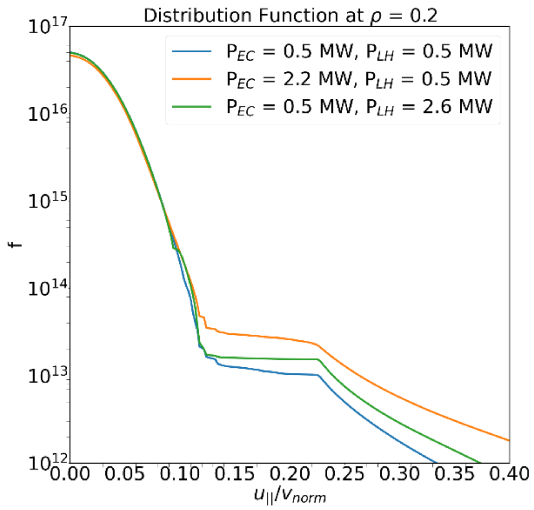

Figure 25. A 1D cut of the electron distribution function at the flux surface of ρ = 0.2 for the case of the maximal synergistic current generation with the toroidal injection angle = 210° and the poloidal injection angle = 76°.

As for future work, it will be interesting to explore if the velocity space interaction between ECCD and LHCD can serve as a method to control LHCD power damping, in addition to the benefit of generating

extra currents. Figure 23 (c) hints at such a possibility with a more localized RF profile. On FTU, internal transport barriers at a larger minor radius were demonstrated with off-axis ECCD, which provided resonant target electrons to promote off-axis LHCD [10]. With resonant electrons provided by ECCD, LHCD could effectively generate a localized current drive off-axis. Additionally, the direct interaction of the LH-resonant fast electrons ($v_{\parallel} = c/n_{\parallel,LH}$) with the EC waves ($n_{\parallel,EC} = c\, k_{\parallel,EC}/\omega_{0,EC}$), can be explored in the so-called down-shifted regime [58,59]. Due to the relativistic effect of the LH-driven fast electrons ($\gamma = 1/\sqrt{1-\left(\frac{1}{n_{\parallel,LH}^2}\right)}$), the EC resonant frequency could be either down-shifted or up-shifted for these LH-resonant electrons, in addition to the Doppler effect. One may control EC power absorption between thermal and LH-driven fast electrons by adjusting the injected EC and LH parallel wavenumbers and the operating magnetic field. This will be explored on EAST in future work. In addition to EAST, the WEST and DIII-D tokamaks will soon be equipped with a combination of LHCD and ECCD systems [60,61]. Beyond the scenario development aspects discussed here, the combined use of LHCD with ECCD may also be tested to control neoclassical tearing modes in the off-axis region where the ECCD efficiency deteriorates, as recently pointed out by [62,63]. LHCD was previously shown to stabilize neoclassical tearing modes on COMPASS-D [64]. There is potential for the combined use of LHCD and ECCD to provide a localized RF current drive source with greater efficiency.

6. Summary

This paper presents kinetic modeling and analyses of the synergistic interaction between LHCD and ECCD using the EAST plasma parameters. The discharge of interest features a high central temperature of 6.5 keV, which supports on-axis LH power damping overlapping with EC resonance—a prerequisite condition for synergistic interaction. This analysis incorporates the impact of collisional dissipation and fast-electron radial transport on synergy interaction. The GENRAY/CQL3D ray-tracing/Fokker-Planck code package is used to construct self-consistent RF quasi-linear diffusion coefficients. Combined with edge/SOL parasitic LH power dissipation, a moderate level of spatial diffusion of fast electrons, in line with experimental expectations, can reproduce the experimental RF current magnitude. When spatial diffusion of fast electrons is included, the region of synergy current generation expands spatially and becomes a smooth profile rather than remaining localized near the peak LH and EC power deposition region. In the high central temperature plasma, core Landau damping occurs within a few passes in the on-axis region, thereby reducing the sensitivity of the LHCD damping profile to the LH wave scattering effect, unlike in a low-temperature, multi-pass damping regime. Including LH scattering effects and radial diffusion broadens the radial region of synergy current generation. For the experimental power level, the synergy current fraction could be up to 10 % of the total current under various conditions considered here.

A parametric scan of ECCD injection angles shows that the toroidal injection angle, which strongly affects the EC wave $n_{\parallel}$, plays more of a role than the poloidal injection angle in the synergy current generation. In our scan, maximal synergy current generation occurs when the overlap of two wave powers is maximized in both the physical and phase space. The study also suggests that the ECCD efficiency at an off-axis location could be sustained at a level comparable to that of the on-axis ECCD when considering the synergy current contribution. Furthermore, the wave power dependence of synergy current generation shows that increasing LH power raises the synergy factor while reducing the

total synergy current fraction. Conversely, increasing EC power increases the total synergy current fraction while the synergy factor itself remains relatively constant. ECCD has minimal impact on the electron distribution function but can couple to LHCD through an overlap in the momentum and position spaces. The power and injection angle scans suggest that proper accounting for the phase space interaction will be essential for the EAST analysis and scenario development, particularly for off-axis RF drive.

While the synergy current fraction in the plasma scenario considered here is relatively modest, future EAST experiments are likely to have increased available LH and EC powers, and the synergy current is expected to be increased as well. The study implies that a synergistic interaction between LHCD and ECCD may offer another way to control the LHCD profile in present-day LHCD experiments where damping is not easily localized in the position space at a relatively low temperature.

Acknowledgments

Work has been supported by the DoE Grant No. DE-SC0010492 and by the National Natural Science Foundation of China (Grant No.11975266 and 11775259). The simulations were performed on the Engaging cluster funded by DoE Grant No. DE-FG02-91-ER54109.

References

[1] N. J. Fisch, Physical Review Letters **41**, 873 (1978).
[2] N. J. Fisch *et al.*, Physical Review Letters **45**, 720 (1980).
[3] P. T. Bonoli, Physics of Plasmas **21**, 061508 (2014).
[4] F. Najmabadi *et al.*, Fusion Engineering and Design **80**, 3 (2006).
[5] B. N. Sorbom *et al.*, Fusion Engineering and Design **100**, 378 (2015).
[6] R. T. Mumgaard, Lower Hybrid Current Drive on Alcator C-Mod: Measurements with an Upgraded MSE Diagnostic and Comparisons to Simulation, PhD Thesis, Massachusetts Institute of Technology, 2015.
[7] A. M. Garofalo *et al.*, Nuclear Fusion **57**, 076037 (2017).
[8] R. H. Cohen, The Physics of Fluids **30**, 2442 (1987).
[9] I. Fidone *et al.*, The Physics of Fluids **27**, 2468 (1984).
[10] C. Castaldo *et al.*, 29th EPS Conference on Plasma Phys. and Contr. Fusion **26B, o-1.04**, (2002).
[11] V. P. Ridolfini *et al.*, Nuclear Fusion **43**, 469 (2003).
[12] G. Giruzzi *et al.*, Phys. Rev. Lett. **93**, 255002 (2004).
[13] M. H. Li *et al.*, Nuclear Fusion **63**, 046019 (2023).
[14] X. M. Zhai *et al.*, Physics of Plasmas **26**, 052509 (2019).
[15] W. Choi *et al.*, Physics of Plasmas **28**, (2021).
[16] M. Q. Wu *et al.*, Nuclear Fusion **58**, 046001 (2018).
[17] F. K. Liu *et al.*, Fusion Engineering and Design **113**, 131 (2016).
[18] M. H. Li *et al.*, Physics of Plasmas **23**, 102512 (2016).
[19] M. Li *et al.*, Nuclear Fusion **62**, 126055 (2022).

[20] H. Xu *et al.*, Fusion Engineering and Design **164**, 112222 (2021).
[21] X. Z. Gong *et al.*, Nuclear Fusion **62**, 076009 (2022).
[22] Y. Song *et al.*, Sci. Adv. **9**, eabq5273 (2023).
[23] A. Smirnov *et al.*, Bull Amer. Phys. Soc **39**, 1626 (1994).
[24] R. W. Harvey *et al.*, in *Proc. of IAEA Technical Committee Meeting on Advances in Simulation and Modeling of Thermonuclear Plasmas* (IAEA, Vienna (1993), 1992), p. 527.
[25] P. T. Bonoli *et al.*, Physics of Plasmas **15**, 056117 (2008).
[26] K. Ushigusa, Plasma Physics and Controlled Fusion **38**, 1825 (1996).
[27] L. L. Lao *et al.*, Nuclear Fusion **25**, 1611 (1985).
[28] S. Shiraiwa *et al.*, Fusion Engineering and Design **112**, 835 (2016).
[29] C. F. F. Karney *et al.*, The Physics of Fluids **22**, 1817 (1979).
[30] C. F. Kennel *et al.*, The Physics of Fluids **9**, 2377 (1966).
[31] M. H. Li *et al.*, AIP Conference Proceedings **2254**, 080005 (2020).
[32] F. K. Liu *et al.*, Nuclear Fusion **55**, 123022 (2015).
[33] S. Shiraiwa *et al.*, in *AIP Conference Proceedings* (AIP Publishing, 2015), p. 030016.
[34] G. M. Wallace *et al.*, Physics of Plasmas **17**, 082508 (2010).
[35] R. W. Harvey *et al.*, Phys. Rev. Lett. **88**, 205001 (2002).
[36] H. Xu *et al.*, Plasma Science and Technology **18**, 442 (2016).
[37] B. J. Ding *et al.*, Nuclear Fusion **53**, 113027 (2013).
[38] P. L. Andrews *et al.*, The Physics of Fluids **26**, 2546 (1983).
[39] P. T. Bonoli *et al.*, Physics of Fluids **25**, 359 (1982).
[40] B. Biswas *et al.*, Plasma Physics and Controlled Fusion **62**, 115006 (2020).
[41] C. S. Liu *et al.*, Physics Reports **130**, 143 (1986).
[42] M. Porkolab, The Physics of Fluids **20**, 2058 (1977).
[43] S. G. Baek *et al.*, Plasma Physics and Controlled Fusion **55**, 052001 (2013).
[44] F. Napoli *et al.*, Plasma Physics and Controlled Fusion **55**, 095004 (2013).
[45] S. G. Baek *et al.*, Physical Review Letters **121**, 055001 (2018).
[46] C. Castaldo *et al.*, Plasma Physics and Controlled Fusion (2024).
[47] R. Cesario *et al.*, Nature Communications **1**, 55 (2010).
[48] Y. Takase *et al.*, The Physics of Fluids **26**, 2992 (1983).
[49] S. Succi *et al.*, Plasma Physics and Controlled Fusion **27**, 863 (1985).
[50] C. Castaldo *et al.*, Physics Letters A **230**, 336 (1997).
[51] R. Cesario *et al.*, Physical Review Letters **92**, 175002 (2004).
[52] Y. Peysson *et al.*, Plasma Physics and Controlled Fusion **58**, 044008 (2016).
[53] N. Bertelli *et al.*, Plasma Physics and Controlled Fusion **55**, 074003 (2013).
[54] S. J. Frank *et al.*, Journal of Plasma Physics **88**, 905880603 (2022).
[55] J. C. Wright *et al.*, Plasma Physics and Controlled Fusion **56**, 045007 (2014).
[56] S. J. Frank *et al.*, Plasma Physics and Controlled Fusion **64**, 105023 (2022).
[57] S. G. Baek *et al.*, Nuclear Fusion **61**, 106034 (2021).
[58] D. Farina *et al.*, Physics of Fluids B: Plasma Physics **1**, 1042 (1989).
[59] V. P. Ridolfini *et al.*, Nuclear Fusion **45**, 1386 (2005).
[60] L. Delpech *et al.*, Fusion Engineering and Design **186**, 113360 (2023).
[61] S. J. Wukitch *et al.*, in *AIP Conference Proceedings* (AIP Publishing, 2023).
[62] A. H. Reiman *et al.*, Phys. Rev. Lett. **121**, 225001 (2018).
[63] S. J. Frank *et al.*, Nuclear Fusion **60**, 096027 (2020).
[64] C. D. Warrick *et al.*, Phys. Rev. Lett. **85**, 574 (2000).